NEUROSCIENCE

A telencephalon cell type atlas for goldfish reveals diversity in the evolution of spatial structure and cell types

Muhammad Tibi[1]†, Stav Biton Hayun[2]†, Hannah Hochgerner[1]†, Zhige Lin[1], Shachar Givon[3], Osnat Ophir[1], Tal Shay[3], Thomas Mueller[4], Ronen Segev[2,3,5]*, Amit Zeisel[1]*

Teleost fish form the largest group of vertebrates and show a tremendous variety of adaptive behaviors, making them critically important for the study of brain evolution and cognition. The neural basis mediating these behaviors remains elusive. We performed a systematic comparative survey of the goldfish telencephalon. We mapped cell types using single-cell RNA sequencing and spatial transcriptomics, resulting in de novo molecular neuroanatomy parcellation. Glial cells were highly conserved across 450 million years of evolution separating mouse and goldfish, while neurons showed diversity and modularity in gene expression. Specifically, somatostatin interneurons, famously interspersed in the mammalian isocortex for local inhibitory input, were curiously aggregated in a single goldfish telencephalon nucleus but molecularly conserved. Cerebral nuclei including the striatum, a hub for motivated behavior in amniotes, had molecularly conserved goldfish homologs. We suggest elements of a hippocampal formation across the goldfish pallium. Last, aiding study of the teleostan everted telencephalon, we describe substantial molecular similarities between goldfish and zebrafish neuronal taxonomies.

INTRODUCTION

The vertebrates' telencephalon, a part of the forebrain, is responsible for higher cognitive functions such as learning and memory (*1*). After massive lesion to the telencephalon, most nonmammalian vertebrates retain the capacity to perform movements but display major deficits in predicting the outcome of future actions (*2*–*5*). In addition, while other parts of the brain stay relatively conserved among vertebrates, telencephalon size and complexity vary considerably across teleost ray-finned fish, amphibians, and amniotes such as reptiles, birds, and mammals (*6*, *7*). Teleost fish are the largest vertebrate family, represented by around 26,000 species. They diverged from the amphibian and amniotes branches of vertebrates 450 million years ago. Their study therefore provides a unique viewpoint on principles of brain evolution and structure.

However, understanding the evolution of brain structure and cell types across the vertebrates' phylogenetic tree faces a long-debated problem in comparative neurobiology: the evolution of an outwardly grown (everted) telencephalon, which is specific for ray-finned fish (*Actinopterygii*). The anatomy of the everted telencephalon does not resemble inwardly grown (evaginated) brains of nonactinopterygian vertebrates (e.g., reptiles and mammals) (*5*). This makes anatomical comparisons to well-known forebrains of tetrapod challenging and led to a controversy about the actual brain divisions of teleost species and their exact homologies with other vertebrates (*8*, *9*)—when two brain structures can only be defined as being homologous if they derive from the same place of origin.

Moreover, teleost fish, such as goldfish, represent the most modern group of ray-finned fish, and their telencephala show great diversity in terms of brain and behavioral complexity and adaptations to spatial ecologies and lifestyles. Goldfish have several key advantages over other experimental systems (*10*): They are highly tolerant to environmental conditions, and their body size can vary according to the experimental needs, from a few centimeters (~10 g) to more than 25 cm (~1 kg). This led to the use of goldfish in many studies that contributed to fundamental understanding of behavior, from visual processing and color perception (*11*), perception of visual illusions (*12*), hormonal effects on behavior (*13*), vestibular input processing and optokinetic response (*14*), all the way to neural integrators (*15*). A notable example for their study in teleostan physiology and neuroscience is the technique of wireless electrophysiology for recordings from free-swimming goldfish, which recently allowed to find place encoding in the goldfish (*16*, *17*).

However, besides the controversies on developmental homologs, today, there is also no accepted complete mapping of functional counterparts between the teleost and amniotes. For example, the prime region for spatial cognition in amniotes is the hippocampal formation, which forms a distinct structure, where place cells are recorded (*18*, *19*). Lesion studies and electrophysiological recordings found evidence for the location of space representing cells not only in the lateral pallium (*5*, *17*) but also in the medial pallium (*20*) and central telencephalon (*16*). It remains an open question to what extent brain regions in teleosts are homologous, and functionally related, to comparable regions in mammals and other tetrapods.

Here, we argue that debates about the evolutionary interpretations of pallial and subpallial territories should be informed by systematic molecular evidence: Understanding the organization of the

[1]Faculty of Biotechnology and Food Engineering, Technion–Israel Institute of Technology, 3200003 Haifa, Israel. [2]Department of Biomedical Engineering, Ben-Gurion University of the Negev, 8410501 Beer Sheva, Israel. [3]Department of Life Sciences, Ben-Gurion University of the Negev, 8410501 Beer Sheva, Israel. [4]Department of Biology, Montclair State University, 1 Normal Avenue, Montclair, NJ 07043, USA. [5]The School of Brain Sciences and Cognition, Ben-Gurion University of the Negev, 8410501 Beer Sheva, Israel.
*Corresponding author. Email: amit.zeisel@technion.ac.il (A.Z.); ronensgv@bgu.ac.il (R.S.)
†These authors contributed equally to this work.

teleostean telencephalon could be greatly aided by uncovering molecular principles underlying its cellular taxonomy. Therefore, we used an unbiased, transcriptome-wide gene expression analysis approach in the widely accessible teleost goldfish. We combined two transcriptome-wide technologies, single-cell RNA sequencing (scRNA-seq) (*21*) and spatial transcriptomics (ST) (*22*), to generate a molecularly and spatially resolved cell type atlas for the goldfish telencephalon. We identified forebrain territories and revealed genes with axial-patterned expression. In systematic comparison to the most thoroughly investigated forebrain today, the mouse's, we identified several molecularly similar cell types and brain structures in goldfish forebrain. Last, we describe strong correspondence between telencephalon cells of the goldfish and the prime teleostan model in development, zebrafish. Our accessible web resource further facilitates free exploration of gene expression across cell types and spatial context of the goldfish telencephalon.

RESULTS

Goldfish telencephalon cell type atlas at spatial resolution

scRNA-seq enables the comparison of molecular similarity and differences of cell types of a given tissue across species, purely based on genome-wide gene expression profiles (transcriptomes). Furthermore, ST approaches can retain positional information of mRNA molecules across the tissue and enable the spatial mapping of gene profiles. Combining these two techniques, we generated a spatially annotated cell type atlas for the goldfish telencephalon (Fig. 1A).

First, we performed scRNA-seq on the full goldfish telencephalon (see Materials and Methods). From fresh coronal sections of total 10 late adult–stage goldfish, we microdissected lateral, medial, ventral, or anterior telencephalon (Fig. 1B and fig. S1). Each region was dissociated to highly viable cell suspensions, single cells encapsulated to microfluidic droplets (10x Genomics), sequenced, and mapped to the reference genome. Since the goldfish transcriptome lacks annotations, we identified and annotated genes according to orthologs to the mouse (see Materials and Methods). We then assigned cells to putative cell types by their expression profile, summarized in Fig. 1. The genome of the teleost ancestor underwent four whole-genome duplications, resulting in additional goldfish gene paralogs. However, we observed no difference in cluster assignment from including additional goldfish gene paralogs (fig. S2). Therefore, gene paralogs were collapsed, and we use gene names according to the mouse ortholog (e.g., *GAD1a* and *GAD1b* become *GAD1*).

At first, on the basis of known markers (e.g., neurotransmitter transporters *SLC17A7*, *SLC17A6*, and *SLC32A1*), we divided the ~40,000 cells into three main classes: glutamatergic neurons (~23,400 cells), γ-aminobutyric acid (GABA)–releasing (GABAergic) neurons (~8300 cells), and nonneuronal cells (~8500 cells), (Fig. 1C). As expected, the dissection compartments (lateral, ventral, medial, and anterior) differed in terms of cell type composition (Fig. 1, D and E, and fig. S1); for example, GABAergic cells dominated the ventral telencephalon (subpallium). The general cell classes contained 106 defined transcriptomic cell types (Fig. 1F), where 40 were GABAergic, 48 glutamatergic, and 18 cell types were nonneuronal (i.e., glial and immune cells; fig. S3, see also comparison with mouse below). We discuss neuronal cell types by a number handle according to the hierarchical clustering (i.e., GABA1 to GABA40 and GLUT1 to GLUT48) and additionally highlight 1 to 3 marker genes in the cell type names in figures (e.g., GABA6-PCDH8-ZIC1).

scRNA-seq revealed molecular expression profiles of cells within the dissected goldfish telencephalon regions to generate the cell atlas. However, tissue dissociation for scRNA-seq came at the loss of more refined spatial information, critical for defining topological identity and possible homologies to other species. Therefore, we next performed ST along the telencephalon's anterior-posterior axis (Fig. 1A). ST (Visium, 10x Genomics) is a sequencing-based, transcriptome-wide in situ mRNA detection method; at the loss of cellular resolution, the method retained positional information of mRNA molecules, per 55-μm-diameter capture spots, that are arranged in an array with centers (X-Y) 100 μm apart. We sampled eight 10-μm coronal sections from two goldfish telencephala, each spaced on average 100 μm apart (Z). Thus, at a pixel size of ~100 μm, the ST data include a complete map (image) of each gene's expression in the goldfish telencephalon.

To test whether the transcriptome can reveal spatial patterns and allow us to delineate territories in the goldfish telencephalon, we performed unbiased clustering of the 6710 Visium capture spots we sampled. We obtained 17 "spatial" clusters based on distinct molecular profiles and remapped the cluster assignment to tissue sections (see Materials and Methods and fig. S4). Although the clustering procedure was dependent solely on gene expression and based on a "bulk" of cells present per 55-μm capture spot, we found clear spatial segmentation in each section. For example, in anterior sections, superficial spots were distinct from all deeper spots. This was likely due to a strong signature of *MFGE8*$^+$ ependymoglia present at the surface proximal to the telencephalic ventricle (ependyma) (fig. S3). More posterior, axial patterning appeared, and some smaller, spatially refined molecular territories became evident, resembling anatomical nuclei.

Spatial mapping of neuronal types for territory parcellation

Noting how ST revealed coarse anatomical parcellations confirmed that transcriptome encodes anatomical information in the goldfish telenecephalon. Moreover, critically, in combination with the scRNA-seq data, the spatial dataset next allowed us to localize molecularly defined neuronal cell types in the telencephalon: To map the probable location of each scRNA-seq cell type to anatomical positions, we applied a cell type mapping algorithm on the spatial dataset (see Materials and Methods). For each molecular cell type, we scored and visualized the detected expression of its top enriched genes per spot in anterior-posterior sections of two replicate brains (fig. S5). Since each spot of the ST array potentially contains on the order of 10 cells, several cell types can map to the same spot. Therefore, we next computed the weighted sum of cell type scores per spot and visualized the integrated mapping of 88 cell types using the cell type colormap of Fig. 1F (Fig. 2A and fig. S6). This mapping allowed a visual identification of the dominant cell types in each spot and provided several key insights: (i) Molecularly related cell types showed overlapping spatial patterns, (ii) all territories were described by a multitude of cell types, and (iii) some territories were clearly distinct from neighbors with sharp borders, contrasting others with more diffuse borders.

For example, glutamatergic types GLUT41 to GLUT48 made up a closely related branch in gene expression and all localized laterally in a territory of the anterior telencephalon only (Fig. 2A, yellow).

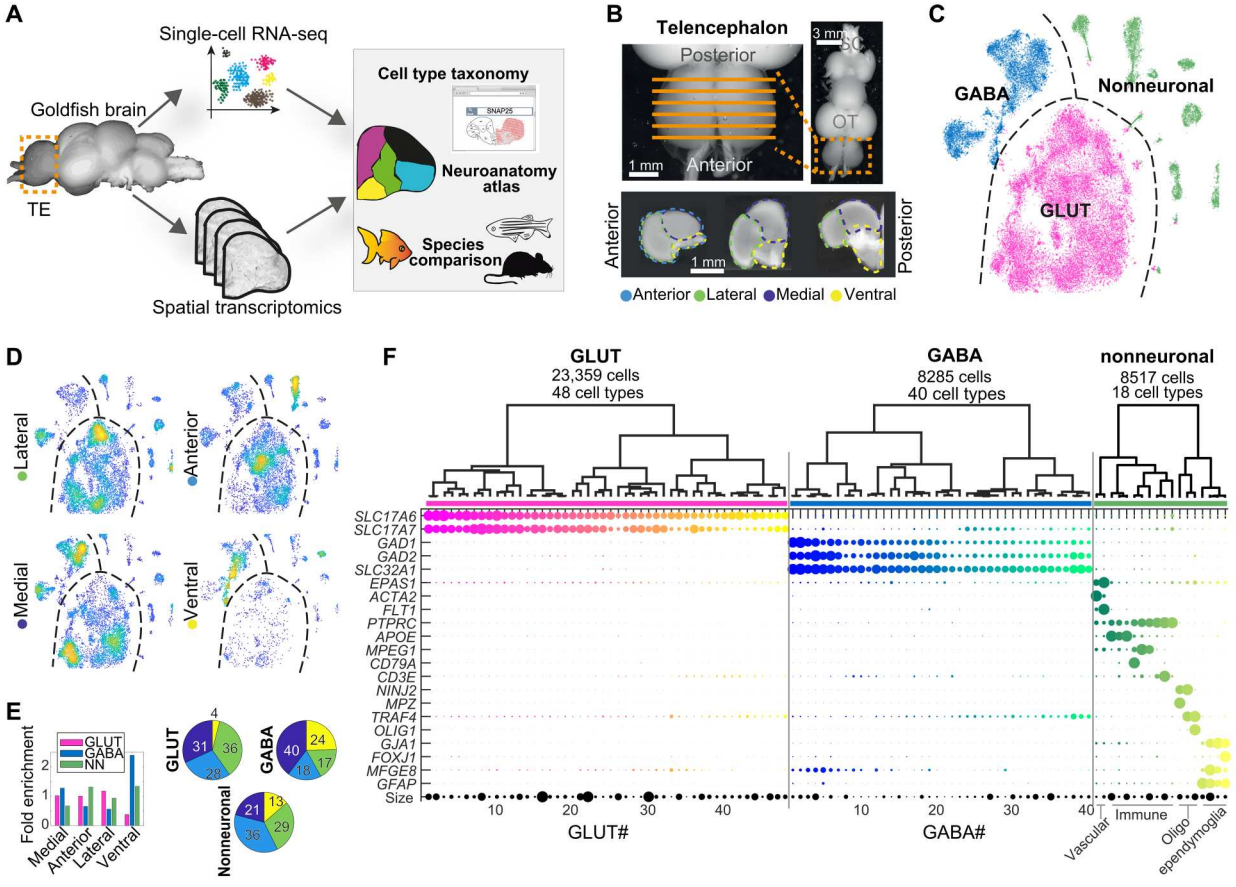

Fig. 1. Composition of goldfish telencephalon cells. (**A**) Outline of this study. Adult goldfish telencephala were analyzed in parallel using spatial- and single-cell transcriptomics, integrated to a spatially mapped cell type atlas, and followed by species comparison. (**B**) Images of fresh dissected goldfish brain and coronal telencephalon sections, describing the microdissection scheme. OT, optic tecum; SC, spinal cord. (**C**) *t*-distributed stochastic neighbor embedding (t-SNE) visualization of all cells in the goldfish forebrain. Each dot represents a cell, colored by class. (**D**) Density scatter visualization on *t*-SNE of all cells [as in (C)] per microdissection origin. Yellow, dense; blue, sparse. (**E**) Left; Contribution of four microdissections to each class; visualized as pie charts. Right: Contribution of cell class to each dissection; visualized as bar plot. (**F**) Dendrogram overview of all cell types. Bottom; Top marker gene expression visualized as dotplot. Dot size represents the percentage of cells in a cluster expressing each gene; dot color represents cell type.

They showed some overlap with the neighboring branch of cell types (GLUT33 to GLUT40); however, the latter continued into more dorsal and posterior sections. Consequently, the border between the anterior-lateral and the more dorsal territories appeared diffused compared, for example, to the sharp border defined by GABAergic clusters GABA24 to GABA40 (green).

Taking advantage of visual color borders, we manually drew regional outlines within each telencephalon Visium section. This resulted in a neuroanatomical delineation based on molecularly defined neuronal cell types. In most cases, we adopted regional names for these defined territories following commonly used terminology for goldfish neuroanatomy (Fig. 2A, bottom) (*23*, *24*). Our anatomical parcellation was astoundingly consistent with traditionally recognized delineations that were mainly based on cytoarchitecture.

Exceptions concern one region not previously annotated [ventral somatostatin (*Vsst*), discussed below] and several annotated territories that we found molecularly indistinguishable. For example, *Dld* (lateral division of area dorsalis, dorsal subdivision) was similar to more posterior *Dp* (posterior division of area dorsalis) and, similar to *Vd* (dorsal nucleus of area ventralis), did not split to *Vs*/*Vp* (supracommissural/postcommissural nucleus of area ventralis) in our annotation. While these distinctions may still be relevant at greater resolution or in other contexts, we resorted to a more simplified annotation.

Unbiased discovery of genes with axial expression

Independent of cell type mapping and regional division, we next aimed to identify genes that carried most weight in spatial segmentation. Spatially restricted genes are of particular interest for species comparisons and understanding developmental origin of cell types. Therefore, we analyzed the topographical distribution of restricted gene expressions according to their medial-lateral and dorsal-ventral axial extent.

To acquire an unbiased spatial score for each gene, we calculated the spread of lateral-medial (X) and dorsal-ventral (Y) coordinates along the spots that express the gene. Genes encoding high spatial information would localize to a specific territory and thus show lower-than-expected spread, as compared to dispersed or sporadic-expressed genes. In addition, just like there may be patterns

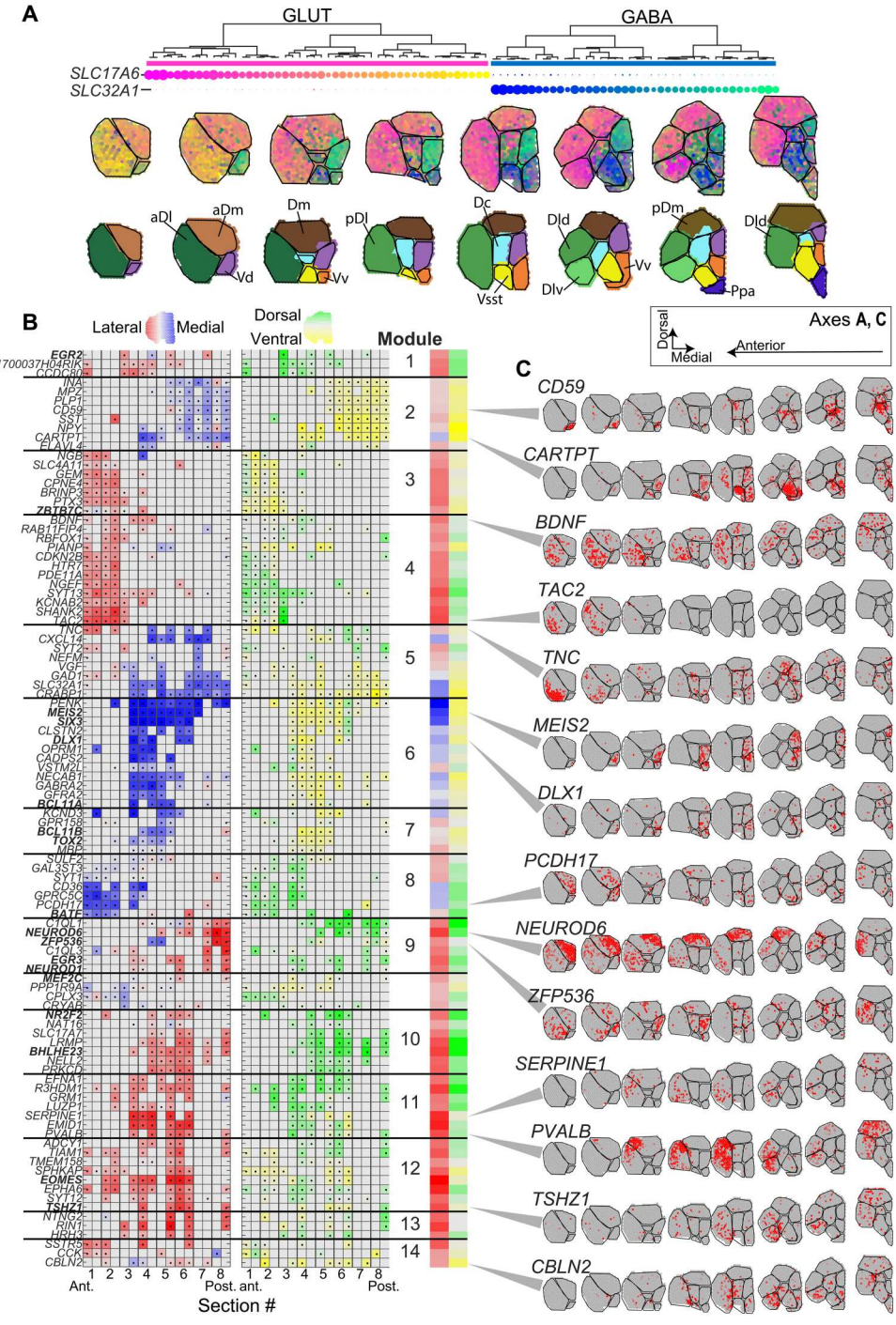

Fig. 2. Axial and regional parcellation of goldfish telencephalon. (**A**) Molecular cell type–based neuroanatomy of the goldfish telencephalon. Top: Color scheme shown above for GABAergic and glutamatergic cell types (dendrogram). Center: Eight coronal goldfish sections (goldfish 1), sampled for Visium ST, overlaid with a weighted color map that integrates all goldfish telencephalon cell types. Bottom: Regional parcellation based on color map differences above, each color indicates a different region, and suggested nomenclature annotated by similarity region names according to Northcutt *(23)*. *D*, area dorsalis; *V*, area ventralis; *Dc*, large-celled subdivision of *Dm*; *Vsst*, ventral Sst; *Ppa*, nucleus preopticus parvocellularis anterioris; a, anterior; p, posterior; d, dorsal; v, ventral; m, medial; l, lateral. (**B**) Heatmaps of SD (normalized per row) along lateral-medial (left) and dorsal-ventral (right) axes for top axial pattern genes, for goldfish 1 and 2; dots indicate spatial enrichment according to axial color scheme shown above; gray without dot, no enrichment. Right: Summary of axial score per gene (mean of enriched sections). (**C**) Expression of 14 axial-patterned genes across the goldfish telencephalon. Gray, low; red, high.

on the *X-Y* plane, certain genes are likely to show anterior-posterior patterns (*Z*) too. This fact may be missed when focusing on a narrower stretch of coronal sections. Therefore, we integrated the *X-Y* spatial scores for all sections and replicates, revealing an aggregated pattern of top highly axial genes along the anterior-posterior axis. Axial patterns were not described by a single gene, but several genes shared similar tendencies, which we grouped to modules. We visualized this systematic, integrated data in Fig. 2B.

We found that axially patterned genes showed coaxial correlation; for example, no gene was patterned only dorsal-ventral, but not medial-lateral. Instead, patterned genes always showed axial enrichment on two or all (*X-Y-Z*) axes. Further, we observed all possible combinations of coaxial relation. For example, modules 3 and 4 were enriched both anterior and lateral and either ventral (module 3) or dorsal (module 4). Neuropeptides *PVALB* (module 12) and *CARTPT* (module 2) were localized lateral-dorsal and medial-ventral, respectively (Fig. 2, B and C); neuropeptide *TAC2* was restricted entirely to anterior-lateral regions. Overall, our systematic scoring of axial-patterned genes can hint at developmental origins (morphogen-like) and serve researchers when designing new genetic lines.

Diverse GABAergic inhibitory cell types

As in recently analyzed nonmammalian species (*25*–*29*), we identify GABAergic cells as those expressing *GAD1*, *GAD2*, and *SLC32A1*, encoding the glutamate decarboxylase enzyme and GABA vesicular transporter, respectively (Fig. 1F). In teleost, these genes are known as subpallial-derived markers. In line with this, our ST data revealed their enrichment in medial, ventral, and posterior regions. Within the GABAergic class, we observed 40 cell types (Fig. 3A), characterized by specific markers (Fig. 3, B and C) and distinct locations in the tissue (Fig. 3D).

First, hierarchical arrangement of the GABAergic cell types on a dendrogram helped reveal their molecular similarities, identify genes that unite related types, and give clues on resemblance to mammals (Fig. 3, B and C). For example, cell types on the rightmost branch of the dendrogram all expressed mammalian striatal markers *MEIS2* and *PENK*, described below. Further, GABA1 to GABA6 cell types shared expression of transcription factors (TFs) *DLX1*, *NXPH1*, and *ETV1* and prepronociceptin *PNOC,* all known as cortical interneuron markers in mouse. In mouse, interneurons show a scattered distribution across the neocortex. Mapping goldfish telencephalon GABA1 to GABA6 cell types to the spatial dataset revealed similarly scattered distributions across the large-celled dorsal subdivision (*Dc*) and *Dl* (Fig. 3, C and D).

Another example is found in the next branch (GABA8 to GABA10), which shared expression of *CPLX1* and *ELAVL4* with GABA1 to GABA6. This related branch also resembled known mammalian inhibitory interneurons by their expression of neuropeptide *SST*. Of these, GABA8 and GABA9 additionally expressed a second neuropeptide, *NPY* (neuropeptide Y). Unlike scattered mouse *Sst* interneurons, however, GABA8 to GABA10 were mainly concentrated in a midventral area in the posterior telencephalon (Fig. 3, C and D). We labeled this ventral domain *Vsst*, after its most abundant cell type (*SST-NPY*) in our region schema (Fig. 2A). Other prominent markers labeling specific mouse interneuron types (*Pvalb* and *Vip*), however, behaved entirely different in goldfish telencephalon: They were not specific to interneurons (GABA1 to GABA10) or even the GABAergic class. For example, the only GABAergic *VIP* population (GABA30) expressed no other markers of local interneurons. This cell type was located in the *Vd* compartment (Fig. 3B and figs. S5 and S9), a region we found enriched for neurons resembling an inhibitory projecting class [medium spiny neurons (MSNs), discussed below]. In addition, the developmental subpallial divisions of ganglionic eminence–derived interneurons were ambivalent in the adult goldfish. Many of the distinguishing markers described in mammals [e.g., medial ganglionic eminence (MGE): *Sst* and *Pvalb*; caudal ganglionic eminence (CGE): *Vip*, *Lamp5*, and *Sncg*] showed overlapping expression (fig. S8, discussed below).

GABAergic types GABA11 to GABA40 were distributed along the midline, with GABA11 to GABA22 in the ventral nucleus of area ventralis (*Vv*) and GABA24 to GABA40 dorsally (*Vd*) enriched. Among them, a small population (GABA15) resembled mammalian dopaminergic neurons: They specifically expressed marker genes *TH* (tyrosine hydroxylase), *SLC6A3* (dopamine vesicular transporter), and *SP8*, a pan-interneuron TF in mouse. Spatially, this cell type appeared in a tiny, ventral-medial nucleus (Fig. 3B and fig. S5), greatly resembling *th1* expression described in zebrafish telencephalon (*30*).

The final *Vd* clade (GABA24 to GABA40) was marked by several prominent markers enriched in a projecting GABAergic class termed MSN in mouse striatum, including TFs *SIX3* and *MEIS2*, neuropeptide *PENK*, and dopamine receptor *DRD2* (but not *DRD1*). This raised a possible analogy between the mammalian striatum and these particularly diverse and discrete goldfish types. Last, we identified putative GABAergic neuroblasts along the periventricular zone at the midline, GABA23. As described for adult neuroblast in fish (*31*) and the axolotl (*28*), this population specifically expressed *MEX3A* and *TUBB5*.

Glutamatergic cell types and their spatial distributions

We found 48 molecularly defined glutamatergic excitatory cell types (Fig. 4, A and B), with distinct, pronounced spatial distributions (Fig. 4C and fig. S5). They were defined by expression of the glutamate vesicular transporter *SLC17A6* (VGLUT2). More than half of these types additionally expressed *SLC17A7* (VGLUT1) (Fig. 1E). This is in notable contrast to mouse, where *Slc17a6* is reserved almost entirely to the diencephalon, *Slc17a7* dominates the forebrain, and only a minority of cell types coexpress the two transporters (e.g., cortex L5, retrosplenial cortex, and some amygdaloid nuclei) (*32*, *33*). In goldfish, *SLC17A6*$^{+}$*SLC17A7*$^{+}$ clusters were present in all territories with glutamatergic expression, but they were sparse in anterior *Dl* (*aDl)* and *Dld*. However, all goldfish telencephalon glutamatergic cells were also marked by *TBR1*, a TF that, in the adult mouse, marks cortical-pyramidal and, to a lesser extent, subcortical-pyramidal neurons (*33*). Glutamatergic cell types were abundant in pallial territories of the dorsal and lateral telencephalon (e.g., *Dm, Dc*, and *Dl*), with an almost complementary spatial pattern to GABAergic cells that were highly abundant in subpallial regions (e.g., *Vv* and *Vd*) (figs. S5 and S6).

The first hierarchical division in glutamatergic neurons was reflected in gene expression and spatial distribution: Here, reelin (*RELN*), cannabinoid receptor 1 (*CNR1*), and thyroid hormone nuclear receptor (*NR2F2*) defined branches of related cell types, with high specificity to the right (GLUT20 to GLUT48: *RELN* and *CNR1*) and left (GLUT1 to GLUT19: *NR2F2*) sides of the dendrogram, respectively (Fig. 4, B and C). These genes also showed

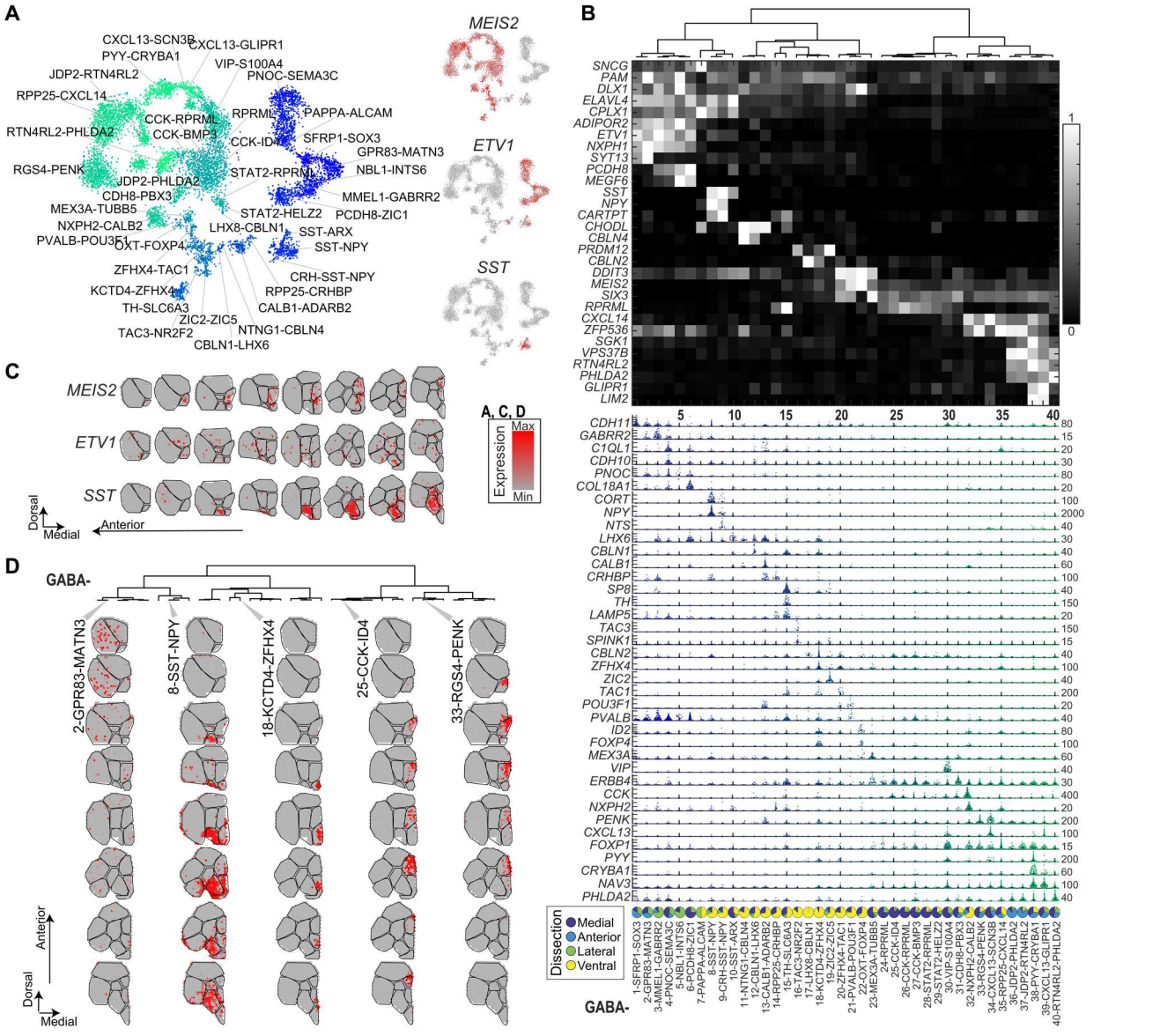

Fig. 3. GABAergic neurons in the goldfish telencephalon. (**A**) *t*-SNE visualization of GABAergic neurons in the goldfish forebrain. Each dot represents a cell, colored by cell type assignment. Right: Expression of three branch-organizing genes. (**B**) All GABA types arranged in dendrogram order (GABA1 to GABA40), with top marker gene expression visualized as heatmap (white, high; black, low). Middle: Violin plots, where each dot represents a single cell; maximum expression (UMI) indicated on the right. Bottom: Contribution of four microdissections to each cell type, visualized as pie charts. (**C**) Expression of three branch-organizing genes [as (A)] and, in ST, eight anterior-posterior telencephalon coronal hemisphere sections. (**D**) Examples across the GABAergic dendrogram for spatial correlation of Visium spots: five scRNA-seq cell types (columns) across eight a.-p. coronal sections (rows).

distinct spatial patterns, with little mutual overlap: *CNR1* was anterior and in *Dm* regions, while *NR2F2* was more posterior in *Dl* and *Dm* (Fig. 4C). *NR2F2*-type GLUT1 to GLUT19 were subdivided into five distinct groups (Fig. 4B). For example, GLUT1 to GLUT6 expressed *BCL11B* and populated the ventral Dl (Fig. 4, B to D, and fig. S5). GLUT7 to GLUT9 had a spatial pattern located in the dorsal part of the goldfish telencephalon *Dm* and *Dc* (fig. S5). The second branch of the dendrogram (*CNR1* GLUT20 to GLUT48) was divided into six distinct groups (Fig. 4B). For example, GLUT29 to GLUT32 expressed *NEUROD1* and *NOCT* and were found in the anterior *Dm*; GLUT41 to GLUT48 expressed *EOMES* and were located in the *aDl* (Fig. 4, B to D, and fig. S5).

GLUT14 and GLUT15 localized to the ventral-most aspects of the posterior telencephalon (fig. S5) and expressed the TF *OTP* and the tripeptide hormone *TRH*. In mouse, these genes faithfully mark several excitatory peptidergic neurons in the mouse hypothalamus and striatal amygdala (*32*–*34*). Last, we observed a population of glutamatergic neuroblasts: GLUT26 expressed *MEX3A* and *TUBB5*, similar to the GABAergic neuroblasts (GABA23) did. Unlike GABA23, which was restricted to the midline, the glutamatergic neuroblasts lined the full extent of the telencephalon's

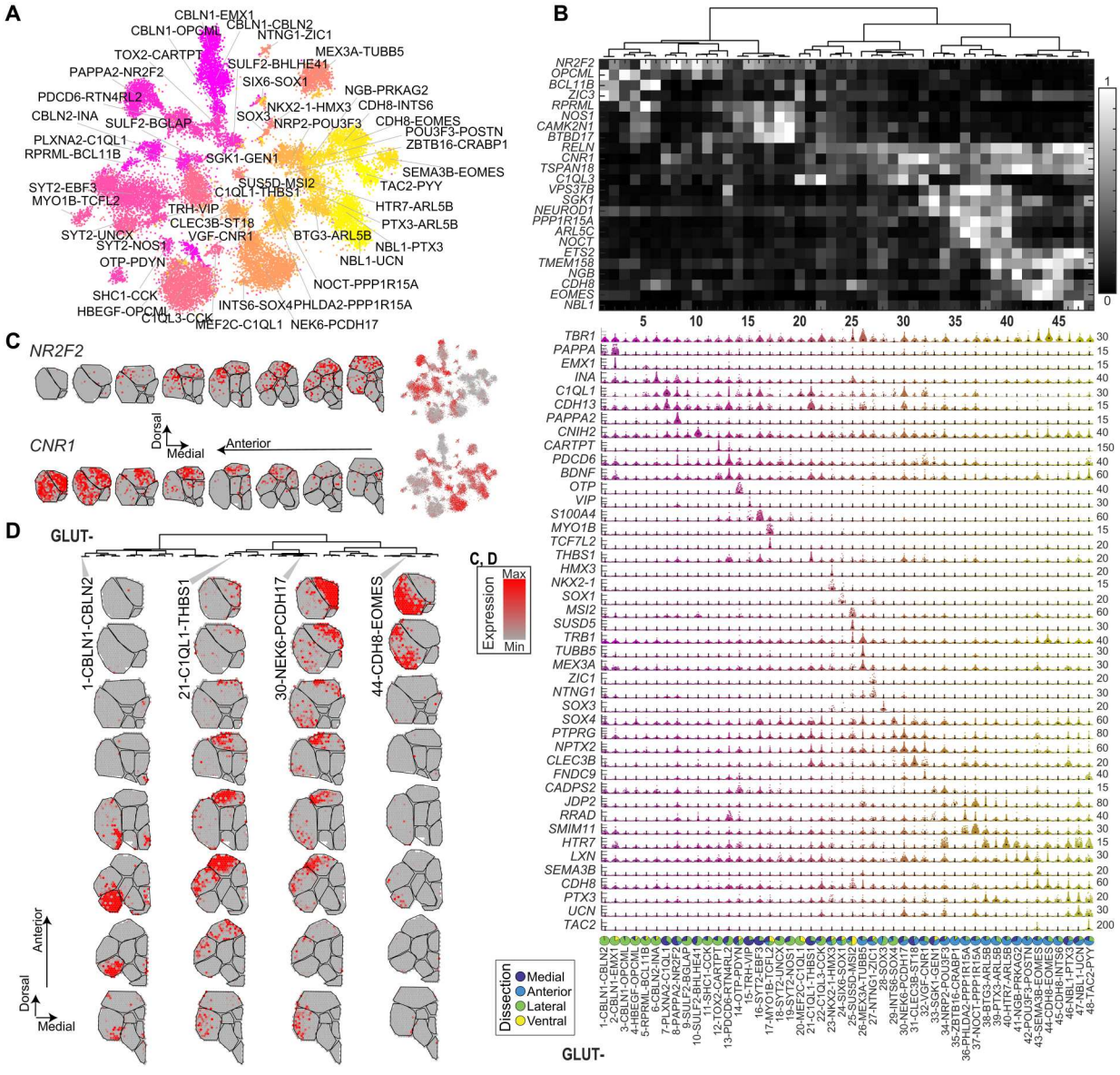

Fig. 4. Glutamatergic neurons in the goldfish telencephalon. (**A**) *t*-SNE visualization of glutamatergic neurons in the goldfish forebrain. Each dot represents a cell, colored by cell type. (**B**) All glutamatergic types, in dendrogram order (GLUT1 to GLUT48), with top marker gene expression visualized as heatmap (white, high; black, low). Middle: Violin plots, where each dot represents a single cell; maximum expression (UMI) indicated on the right. Bottom: Contribution of four microdissections to each cluster, visualized as pie charts. (**C**) Expression of two branch-organizing genes, *NR2F2* and *CNR1*, visualized on *t*-SNE [as (A)] and, in ST, eight anterior-posterior telencephalon coronal hemisphere sections. (**D**) Examples across the glutamatergic dendrogram for spatial correlation of Visium spots: four scRNA-seq cell types (columns) across eight anterior-posterior coronal sections (rows).

ependyma (fig. S5). This pattern notably resembled the distribution of goldfish ependymoglia (e.g., *HES5*$^{+}$ *and MFGE8*$^{+}$; see fig. S3) that were most proximal to the telencephalic ventricle. Astrocyte-related *Hes5*$^{+}$ radial glia act as adult neurogenic stem cells in the mouse (*35*). Together, these cell types therefore likely constitute the periventricular neurogenic niche in the adult goldfish telencephalon (*36*, *37*).

Molecular signatures of teleost telencephalon parcellation

Our analysis of axially patterned genes (Fig. 2) and molecular cell type mapping (Figs. 3 and 4) allowed to molecularly define regional boundaries. To ease future functional exploration, we next asked the reverse question: Which genes (Fig. 5, A and B) and cell types (Fig. 5C) best defined each compartment? For example, the *SST*-dominated nucleus *Vsst* described above was also defined by SST receptor-binding cortistatin (*CORT*). TF eomesodermin *EOMES* (also known as TBR2) neatly labeled the aDl. Calcium-binding *NECAB2*, a modulator of the adenosine 2A and mGluR5 receptors, was not only concentrated in the ventral subdivision of lateral division of area dorsalis (*Dlv*) but also dispersed, for instance, across the *pDm*. In contrast, white matter–dominated *Dc* was indeed best described by myelin-binding protein *MBP* and enriched for

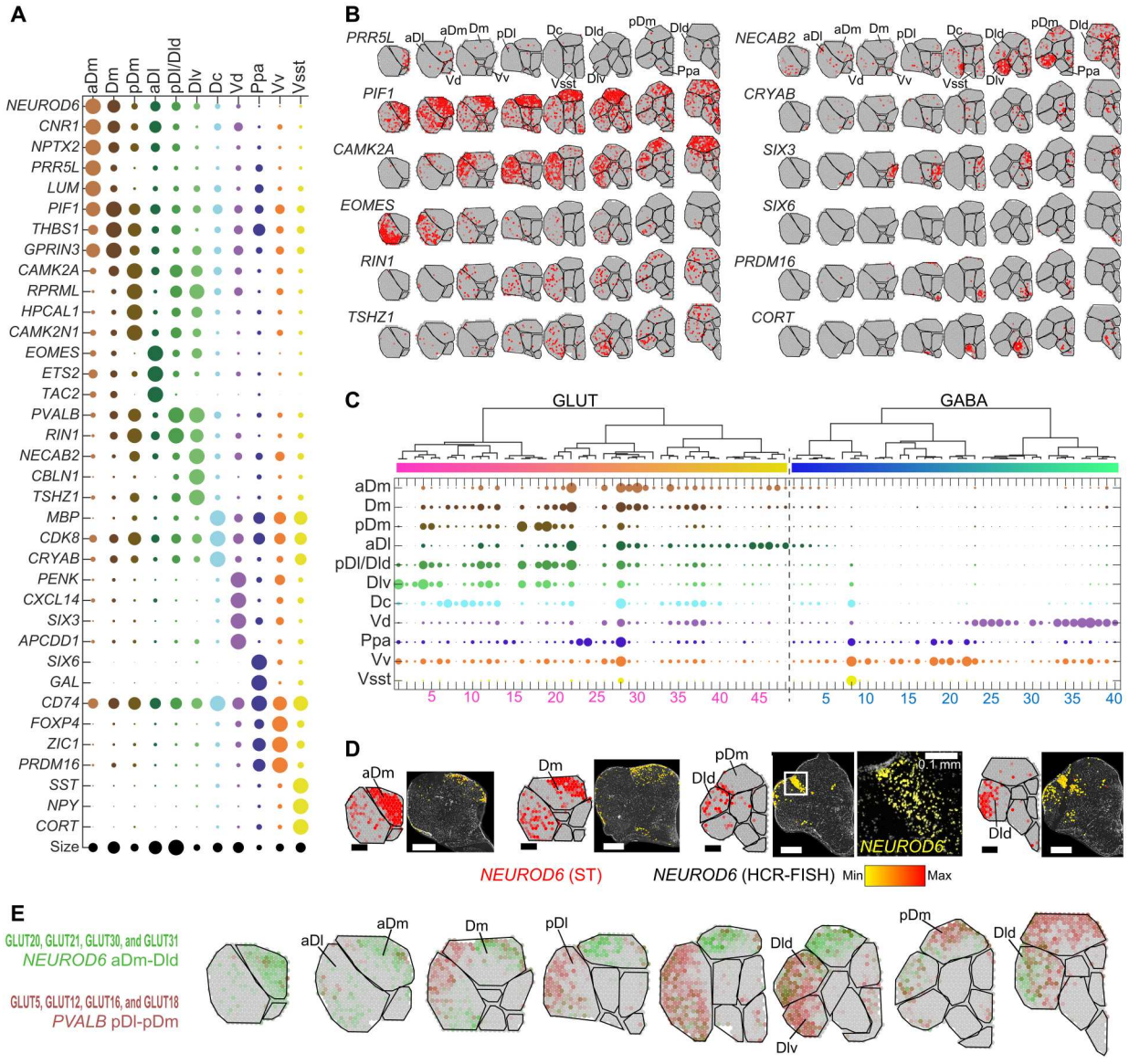

Fig. 5. Region-specific marker genes and cell types. (**A**) Top enriched region-specific marker genes as identified by ST, presented as dotplot: Circle size represents normalized mean expression of each gene in each region. (**B**) Representative examples of genes from (A), with spatial distribution of expession across eight anterior-posterior telencephalon sections. Gray, low; red, high. (**C**) Enrichment of cell types to regions shown as dotplot, where dot size represents the correlation between cell type expression profile and region expression profile. (**D**) Validation of a switch in territories for *NEUROD6* expression along the telencephalon anterior-posterior axis in matched sections of ST and HCR-FISH. Section overviews for HCR are displayed segmented, with normalized expression scale below. Scale bars, 0.5 mm (ST and HCR-overview). (**E**) Weighted spatial cell type enrichment for two groups of glutamatergic clusters only (green, GLUT20, GLUT21, GLUT30, and GLUT31; red, GLUT5, GLUT12, GLUT16, and GLUT18), indicating a *Dm-Dl* territory switch for both groups that would result in 3D bends/horns.

oligodendrocyte populations. Together, this analysis pinpointed genes that precisely described the molecular base consistent with known anatomical delineations.

Excitatory cell types with a "twist" to axial parcellation

Multiple data points in our analysis emphasized the importance of molecular characterization along the full anterior-posterior axis to better recapitulate underlying structures in three dimensions (3D). For example, we found interesting changes in gene expression and cell type composition between the anterior versus posterior pallium in both the *Dm* and *Dl* regions. First, we noticed that *NEUROD6*, a gene known to mark hippocampus pyramidal neurons in mammals, was dorsomedial in anterior sections (*aDm* and *Dm*) but posterior, appeared to "switch" territory to *Dld* [corresponding to Northcutt (*23*) *Dp*] (Figs. 2C and 5D). Notably, neuropeptide *PVALB* appeared to make the opposite switch, where, more anterior, it was localized dorsolateral (*Dl*/*pDl*) but posterior in the dorsomedial zone (*pDm*) (Fig. 2C). This trend was reflected by additional genes that shared axial-patterned expression with *PVALB* and *NEUROD6* (e.g., for *PVALB*, *CAMK2A*, *EFNA1*, *SERPINE1*, and *EMID1*) (Figs. 2B and 5B). Spatial distributions of several glutamatergic cell types supported this observation too: Along the anterior-posterior axis, GLUT20,

GLUT21, GLUT30, and GLUT31 switched from *Dm* to *Dld*, while GLUT5, GLUT12, GLUT16, and GLUT18, switched from *Dl* to *pDm* (Fig. 5E and fig. S5).

Parcellations purely based on axial divisions were thus not always consistent with patterning based on cell type. If gene expression and cell type composition represent functionality, then the medial-lateral *Dm-Dl* transitions described here deserve attention: We propose that in the current example, the two groups of neuronal populations potentially represent distinct functional units, described by *NEUROD6* (*Dm-Dld*) and *PVALB* (*Dl-pDm*). In three dimensions, each group would form a bend or horn, analogous to the 3D shape of the rodent hippocampus. Together, these bends would look intertwined, resembling an anterior-posterior twist of two molecularly and functionally distinct territories.

Molecular similarities of cell types between goldfish and mouse

The structure of the forebrain is diverse across different vertebrates. Today, the mouse brain is of central importance to our understanding of vertebrate nervous systems, but it diverged from teleost about 450 million years ago. Comparative studies on telencephalon of amphibians (*26*–*28*), bearded dragons (*29*), and turtles (*25*) reveal deeply conserved cell types, even when compared to the mouse brain. Given their vast evolutionary distance, identifying molecular similarities and homologous brain regions between goldfish and mouse may be challenging but could lead to a better understanding of the evolution of vertebrate brain structure. We therefore continued our investigation of the goldfish telencephalon with systematic comparison to the mouse forebrain. Briefly, we integrated our goldfish taxonomy with a published mouse telencephalon cell type taxonomy (*33*). For this purpose, we merged the species′ datasets to mixed-species datasets of nonneuronal cells, GABA neurons, and GLUT neurons. For each cell class separately, we performed feature selection and dimensionality reduction and iterated the data integration tool Harmony (*38*) until embedding of the two species′ cell atlases converged (see Materials and Methods and fig. S7). We then applied two parallel approaches aiding comparative analysis: (i) clustering to mixed-species pseudo–cell types and (ii) a KNN (*k*-nearest neighbor) classifier of goldfish cells to mouse cell types (Fig. 6A).

To circumvent biases inherent to each of the methods (e.g., cluster size dependency), we present examples of cell types that were in consensus between the two methods, that is, where both approaches identified mouse-goldfish similarities (Fig. 6 and fig. S7). Then, we examined the spatial mapping of these conserved neuronal cell types to assess to what extent also spatial confines, or brain regions, may have been conserved.

Conservation of glial cells and an expansive goldfish immune niche

Nonneuronal cells showed an overall large degree of conservation between the two species, with some interesting exceptions. Among glial populations, we detected three types of ependymoglia that are all closely related to the diverse mouse astrocyte populations (Fig. 6, B and C, and fig. S7). They expressed a palette of known mammalian astrocyte markers, including *MFGE8*, *GFAP*, and *GJA1* (fig. S3). In line with functional differences between the teleost and mammalian counterparts (*39*, *40*), goldfish ependymoglia expressed genes not typically detected in mouse astrocytes, e.g., metallothionein *MT4,* delta-like notch ligand *DLL1,* monocarboxylate transporter *SLC16A9*, and secreted glycoprotein *SLIT2* (with axon guidance functions in development) (fig. S3). In addition, unlike in mammals, all populations were almost entirely restricted to the pial and ventricular surfaces (fig. S3). The population that expressed mouse radial glia marker *HES5* (ependymoglia-*HES5-DLL1)* are indeed closely related to both radial glia populations of the two neurogenic niches of the adult mouse, dentate gyrus, and subventricular zone (Fig. 6B). Ependymal cells were very closely related between the species in both gene expression and distribution along the ventricles (Fig. 6B and figs. S3 and S7). This is expected given their necessarily conserved function in circulating cerebrospinal fluid and the palette of gene products necessary for this specialization.

The goldfish oligodendrocyte niche reconstituted the entire lineage as described for the adult mouse brain, from oligodendrocyte progenitors (OPCs) to committed oligodendrocytes (COPs), and lastly a mature, myelinating oligodendrocyte (Fig. 6B and figs. S3 and S7). This observation cements both a conserved developmental origin and, similar to ependymal cells, their conserved specialized function in myelination. However, goldfish oligodendrocytes also expressed genes such as *CLDN19*, *MPZ*, and *SPARC* (fig. S3), which, in the mouse, are entirely reserved to the myelinating cells of the peripheral nervous system, the Schwann cells (*33*). This is particularly notable given that the mammalian Schwann cells′ developmental origin is in the neural crest, not neural tube. Because of the small amount of Schwann cells included in the mouse dataset, however, this unexpected relationship between mouse Schwann cells and goldfish oligodendrocytes was missed by both approaches in our analysis (Fig. 6, B and C, and fig. S7).

In contrast to the mouse, the goldfish telencephalon immune niche—marked by *PTPRC* (CD45)—was remarkably diverse (fig. S3). Similar to the mouse brain, we detected several types of macrophages (*APOE*) and microglia (*MPEG1*) (Fig. 6, B and C, and figs. S3 and S7). Some immune cells bore similarity to myeloid and lymphoid components of the peripheral immune system not generally detected in the mouse brain, such as granulocytes or monocytes (immune-*CCL2-CCL24* and immune-*AQP1-AQP9*), B cells (immune-*CD79B*), and T cells (immune-*CD3E-SLA2*). Therefore, similarity to the annotated mouse forebrain dataset may be misleading (Fig. 6, B and C, and fig. S7). For example, granulocyte-like immune-*AQP1-AQP9* resembled ependymal (EPMB) and subcommissural (HYPEND) cells in KNN analysis and astrocytes (Bergmann glia) in the clustering approach. The putative T cell immune-*CD3E-SLA2* resembled vasculature (VLMC/ABC) and epithelium (choroid plexus). However, it is tempting to speculate whether this observation points to functional analogies over the evolution of cell types in mouse and goldfish.

Molecular similarity and spatial dissimilarity in SST interneurons

In the GABAergic class, species comparison detected potential conserved cell types, with molecularly similar counterparts in both species (Fig. 6, D to H). First, both KNN and integrated cluster analysis confirmed the overall split between interneurons (GABA1 to GABA10) and putative projecting (MSN-like) inhibitory types (GABA16 to GABA40).

GABA1 to GABA7 resembled a group of cortical and hippocampal interneurons (TEINH14 to TEINH18), a mix of CGE- and

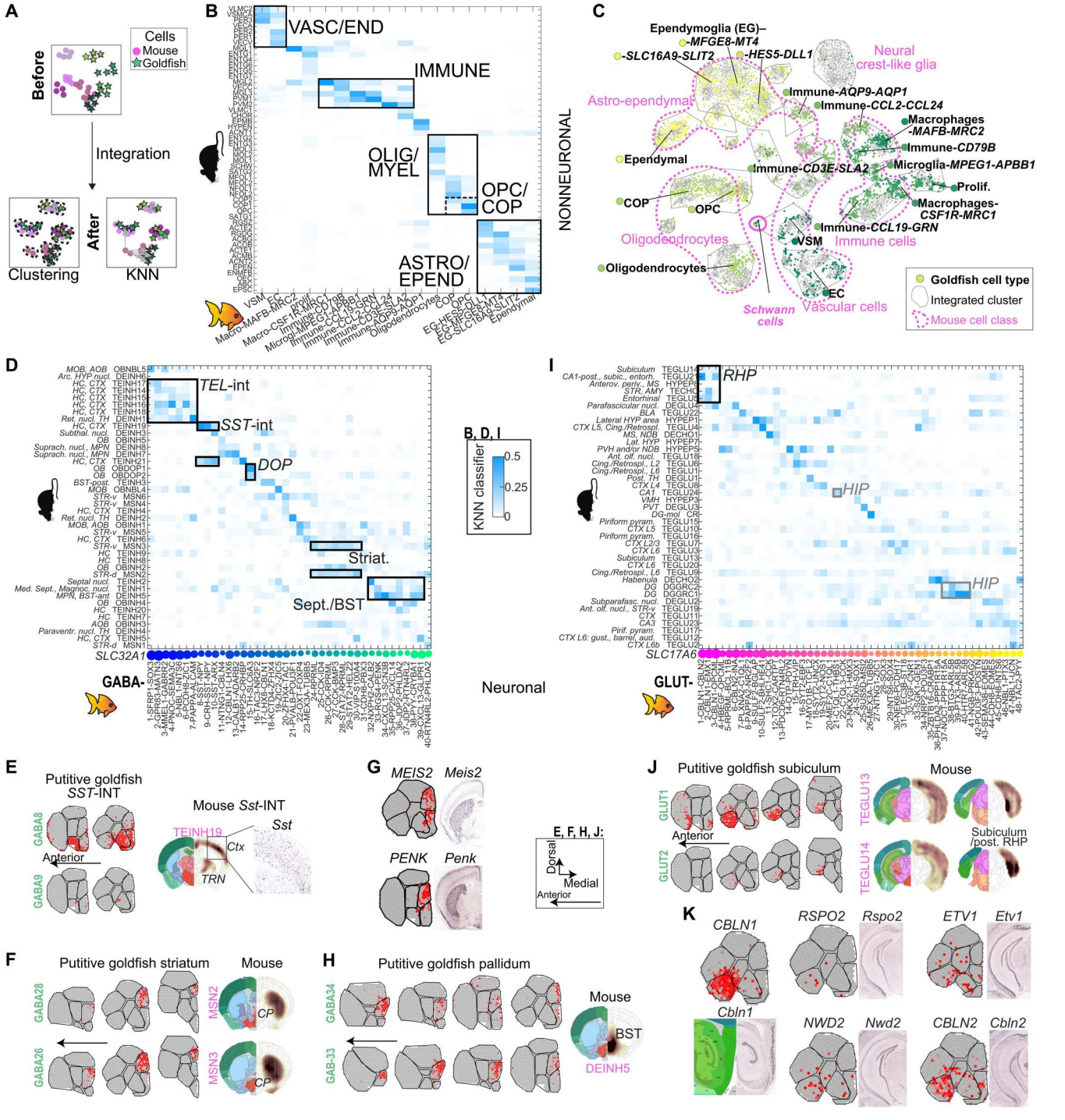

Fig. 6. Goldfish and mouse cross species comparison of the telencephalon cell types. (**A**) Scheme of comparative species analysis between goldfish and mouse telencephalon (*33*). Per cell class, both species' datasets are integrated (Harmony), followed by density-based spatial clustering of applications with noise (DBSCAN) clustering or a KNN classifier. (**B**) Nonneuronal cells species comparison visualized as heatmap with conserved cell types outlined (KNN classifier). (**C**) Nonneuronal cells species comparison visualized as *t*-SNE. Dots represent cells, colored by goldfish cell type. gray, mouse cell; gray outlines, integrated cluster (see fig. S7); pink outlines and labels, mouse cell class; with mouse Schwann cells highlighted. (**D**) GABA class species comparison (KNN classifier), with examples for consistency with integrated clusters highlighted. (**E**) Distribution of *SST* interneuron types by spatial correlation with goldfish ST and mouse ISH (*33*), with zoom-in to dispersed *Sst* expression in isocortex (*58*) (Allen Mouse Brain ISH Atlas). (**F**) Distribution of (putative) striatal neuron types by spatial correlation with goldfish ST (left) and mouse ISH (right) (*33*). (**G**) Expression of two mouse striatum markers in goldfish ST (left) and mouse ISH (right) (*33*). (**H**) Distribution of (putative) pallidal neuron types by spatial correlation with goldfish ST (left) and mouse ISH (right) (*33*). (**I**) GLUT class species comparison (KNN classifier), with examples for consistency with integrated clusters highlighted. (**J**) Distribution of (putative) retrohippocampal neuron types by spatial correlation with goldfish ST (left) and mouse ISH (right) (*33*). (**K**) Expression of five genes in goldfish ST and mouse ISH, in (putative) subiculum/retrohippocampal formation.

MGE-derived phenotypes (Fig. 6D). Goldfish *SST* clusters GABA8 to GABA10 were a particularly notable example of a highly conserved neuron type. Both in integrated cluster and KNN analyses, GABA8 to GABA10 scored closely to mouse cortex SST interneurons TEINH19 and TEINH21 (Fig. 6D and fig. S7). However, as mentioned above, spatial distributions of this neuron type differed in the two species (Fig. 6E): In the mouse, *Sst* interneurons are distributed in a dispersed pattern all over the telencephalon. In the goldfish, we found mapping of *SST* types GABA8 to GABA10 concentrated, and dominating, in the lateroventral portion of the subpallium, a region we termed *Vsst* (Fig. 2A and fig. S6). Both ST and fluorescent in situ hybridization (FISH) showed sparse *SST* expression in the pallium and confirmed our observation of a dense subpallial SST^+ nucleus (Figs. 6E and 7 and fig. S9). Because of their aggregated spatial pattern, we speculated whether the *SST* types may correspond more closely to a different subpallial type, such as the Sst^+ populations of the mammalian striatal amygdala. We integrated all GABAergic populations with an additional mouse amygdala dataset (fig. S8) (*32*). However, the goldfish-*SST* population GABA8 to GABA10 were unrelated to *Sst*-expressing projecting types of the mouse central amygdala (fig. S8). Instead, they closely clustered with amygdala Sst^+ MGE-interneuron populations and, in the case of GABA10, one Sst^+ population of the medial amygdala, all of which also shared expression of migration-regulating TF *Nkx2-1* (fig. S8) (*41*). Together, *SST* interneurons serve as a strong example for a highly molecularly conserved cell type with mouse cortical and subcortical *Sst* interneurons. However, because of their distinct localization, further work will be needed to clarify whether these conditions imply different functionality.

The same analysis also revealed more global ambivalence of goldfish interneuron populations with respect to the developmental origins in the ganglionic eminences (fig. S8). Overall, the two interneuron branches GABA1 to GABA7 and GABA8 to GABA10 mapped closely to CGE and MGE, respectively. In addition, GABA8 to GABA10 *SST* interneurons expressed not only MGE-associated neuropeptide Y (*NPY*) and TF *LHX6* but also CGE-associated genes *SNCG*, *LAMP5*, and *ADAR2B* and TFs *SP8* and *NR2F2*. Similarly, GABA1 to GABA7 expressed not only CGE-associated TFs *PROX1*, *NFIB*, and *NFIX* but also MGE-associated *NXPH1*, *NOS1*, and *PVALB*. In addition, while the global similarities revealed by integrated embedding and expression of conserved TFs may better reflect shared evolution, several atlases in tetrapods [e.g., salamander (*26*) and lizard (*29*)] revealed decidedly higher molecular similarities with mammalian interneuron classes.

Striatal and pallidal derivatives in goldfish Vd

The other branch of goldfish GABAergic cell types (GABA16 to GABA40) overall had less similarity to local inhibitory cortical interneuron types (Fig. 6D). Instead, some of the top correlated cell types in the mouse included striatal medium spiny cells and inhibitory neurons of the mouse septum and pallidum. GABA25 to GABA28 in the goldfish, for example, consistently grouped with mouse MSN (Fig. 6F). ST mapped these cells medial to the Vd (Fig. 2A, purple, and fig. S5). In addition, mouse striatum markers *PENK* and *MEIS2* aggregated exclusively in the goldfish Vd, forming a continuous regional entity resembling the situation in the mouse striatum (Fig. 6G). Last, species comparison consistently aligned GABA33 to GABA39 with mouse septal and pallidal inhibitory cell types and most prominently with bed nuclei of the stria terminalis (BST) population DEINH5 (Fig. 6D and fig. S7). These cell types were localized in more anterior aspects of the *Vd* (Fig. 6H). Together, these similarities in molecular composition and spatial distribution suggest goldfish homologs to mouse cerebral nuclei in the *Vd*. Our analysis further suggests their resolution to pallidal- and striatal-like regions in the *Vd*'s most anterior and posterior aspects (including those traditionally termed *Vs* and *Vp*), respectively.

A suggested retrohippocampal formation homolog in goldfish Dlv

In contrast to GABAergic, and certainly nonneuronal types, glutamatergic cell types showed less coherence between our two approaches to species comparison. This implies lower levels of conservation in the excitatory cell class (Fig. 6, I to K), as was described also for the reptilian pallium (*25*).

Nevertheless, we found that GLUT20 to GLUT22 and GLUT37 to GLUT40 were potentially related to hippocampal neurons: Regardless of the analysis approach, both groups were similar to mouse hippocampus proper (Fig. 6I). However, this relationship could not be pinpointed to single mouse cell types. Instead, depending on the approach, their relation alternated between hippocampal subdivisions of the mouse [e.g., TEGLU24 (CA1), TEGLU23 (CA3), and DGGRC1-2 (DG)] (Fig. 6I, fig. S7, and table S1). The similarity between these cell types in goldfish and mouse may be partly explained by mouse hippocampal–enriched genes *C1QL1* and *NEUROD6,* which were highly expressed in, e.g., GLUT21 and GLUT22. Both groups (GLUT20 to GLUT22 and GLUT37 to GLUT40) were located scattered across the *Dm* and *Dl* regions (fig. S5). Together, these findings hint at limited molecular conservation and a less spatially defined hippocampal-like formation in goldfish compared with the mouse.

Most consistently among glutamatergic neurons, one group of goldfish neurons, GLUT1 and GLUT2, scored closely to subiculum glutamatergic cell type (TEGLU14) (Fig. 6, I and J, and fig. S7). The goldfish cell type counterparts mapped to the molecularly distinct lateral-ventral region spots, *Dlv* (Fig. 6J and fig. S5). The similarity between the species was manifested by their shared expression of *CBLN1*, *CBLN2*, *NWD2*, *ETV1*, and *RSPO2* (Fig. 6K). In addition, KNN analysis only suggested that entorhinal and posterior hippocampal mouse neuron types (TEGLU5 and TEGLU21) were closely related too (Fig. 6I). In mouse, the entorhinal area and subiculum belong to the retrohippocampal formation. They play a major function in hippocampal-cortical interaction and spatial navigation, e.g., head direction (*42*). Together, these putative subiculum, or retrohippocampal formation–like neurons in goldfish, showed conserved molecular profiles and, at the same time, were concentrated in a region (*Dlv*) that, according to teleostean everted telencephalon development, may also correspond to the retrohippocampal formation topologically (*5*).

Teleostean telencephalon homologies in goldfish and zebrafish

Calling of homologs between species relies on the identification of evolutionary topological maps and is therefore greatly aided by detailed understanding of their development. Teleosts such as the goldfish and zebrafish share an everted telencephalon topology. However, the zebrafish (*Danio rerio*) is the most deeply studied teleostean representative and famously comes with a plethora of tools

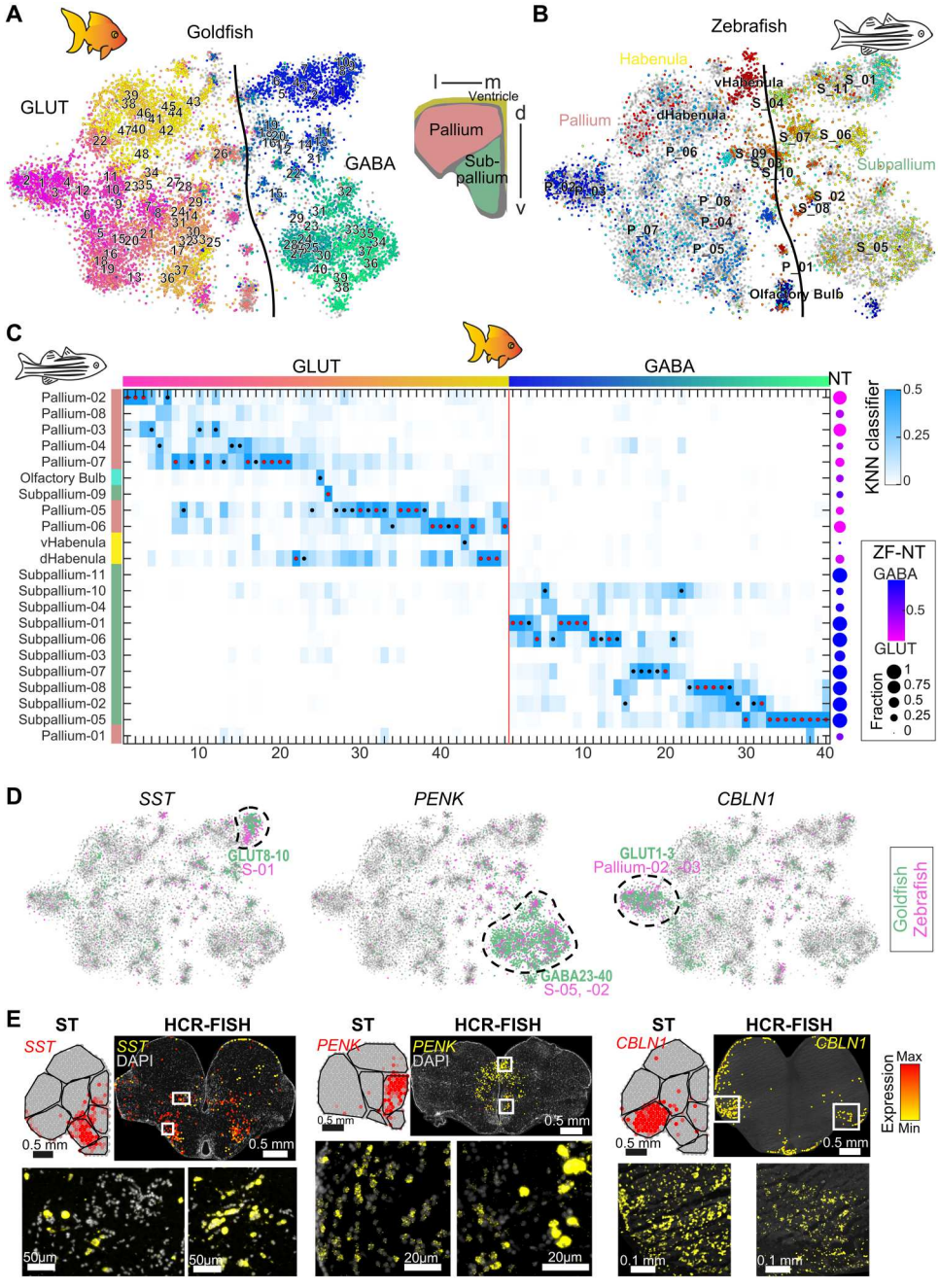

Fig. 7. Cross-species comparison of teleostean telencephalon cell types. (**A** and **B**) *t*-SNE visualizing comparative species analysis between goldfish and zebrafish (*46*) telencephalon, with cell types highlighted per species; (A) goldfish and (B) zebrafish. Per cell class, both species' datasets are integrated (Harmony), followed by DBSCAN clustering. (**C**) Per cell type comparison, scored using KNN classifier. (**D**) Expression of *CBLN1*, *PENK*, and *SST* in the integrated teleostean dataset; dots (cells) colored by species origin. (**E**) Validation of gene expression detected in ST using HCR-FISH. Top row: Corresponding section overviews of genes detected in Visium (left) and HCR (right), where each spot represents a segmented fluorescent cell, colored by normalized expression. Bottom row: Raw fluorescent signal in zoom-ins, as indicated in overview sections.

in the study of its development. Molecular, developmental, and connectivity data in zebrafish have indicated that the topology of the zebrafish telencephalon can be compared to the mammalian situation (*43*–*45*).

Therefore, we next integrated data from an adult zebrafish telencephalon cell type survey (*46*) with the goldfish telencephalon. In this analysis, we took advantage of the relatively better annotated zebrafish transcriptome and used it to annotate goldfish genes, although paralogs resulting from whole-genome duplications were again collapsed (see Materials and Methods). Comparing the 21 zebrafish telencephalon neuronal types with the 88 neuronal types of the goldfish telencephalon revealed a strongly conserved cell

taxonomy between these teleostan species (Fig. 7, A and C), compared to the mouse (Fig. 6 and fig. S7). As expected, cell types that were annotated by Pandey *et al.* (*46*) as pallial, or subpallial, largely divided on the basis of neurotransmitter class, and they were predominantly glutamatergic or GABAergic, respectively.

On the level of cell types, Subpallial_01 corresponded to several goldfish interneuron populations, including the *Sst*-expressing type aggregated in goldfish *Vsst* (Fig. 7, D and E, *SST*). The authors describe similar absence of *VIP* in the zebrafish interneuron class and concluded that in zebrafish, no population corresponded to CGE-derived mammalian interneurons. Medium spiny-like goldfish cells GABA23 to GABA40 resembled zebrafish clusters Subpallium_02 and Subpallium_05 (Fig. 7, D and E, *PENK*). Last, a pallial zebrafish cluster (Pallium_02) bore great resemblance to the putative goldfish homologs of retrohippocampal cell types GLUT1 to GLUT3 (Fig. 7, D and E, *CBLN1*). As in our data, the authors located this population in the Dlv and independently report the same molecular resemblance to mouse subiculum. Although sampling depth, annotation, and spatial mapping hindered more detailed analysis, this comparison confirms that the molecular cell type taxonomy of goldfish telencephalon can facilitate study of other teleosteans.

DISCUSSION

Combining ST with scRNA-seq, we generated a neuronal cell type atlas for the telencephalon of goldfish, a carp-like (cyprinid) teleost fish with outwardly grown (everted) telencephalon characteristic for ray-finned fish (*Actinopterygii*). The resulting datasets will provide a critical resource to analyze neuron type evolution across vertebrates offering to compare huge datasets across various emerging forebrain cell type atlases of mammals (*33*, *47*), reptiles (*25*, *29*), and amphibians (*26*–*28*).

Our study found 88 GABAergic and glutamatergic neuron types alongside accurate spatial mapping. We determined that all major classes of forebrain cell types found in other species also exist in the goldfish. In addition, in a systematic comparison to mouse telencephalon, many neuronal populations had direct counterparts in the mouse, some of which point to conserved brain regions.

ST revealed the expression patterns of thousands of genes. We introduced an efficient way for spatial scoring of axial-patterned gene expression in the telencephalon. This method can be helpful to systematically identify genes with spatially restricted patterns and, thus, inform about potential region-specific extent and anatomical delineations. In our case, it identified top potential markers in the mediolateral and dorsoventral axes. Many of these pattern-forming genes were enriched on all three axes and were thereby in line with current anatomical delineations of molecularly distinct regions or nuclei. These spatially informative genes may also give clues to underlying developmental processes and evolutionary origins of brain structures in vertebrates. For example, follow-up studies could use tracing approaches on TFs that stay spatially informative in the adult telencephalon.

Beyond identifying spatially restricted expression of single genes, we also used ST to map all cell types to their location. Assuming that a molecularly defined neuronal type represents a particular functional unit, we then parcellated the combined map of all cell types to propose a regional neuroanatomy of the goldfish telencephalon. In addition, while this approach was often in agreement with traditional cytoarchitecture-based telencephalon atlases (*23*, *24*), our parcellation revealed a molecular-neuronal and therefore likely functional base for regional divisions. This speculation was supported by several cell types that were molecularly similar in our systematic comparison of goldfish cell types to a mouse telencephalon taxonomy. Here, some molecularly similar neuron types within the goldfish telencephalon hinted at homologies to mouse telencephalon: They showed discrete spatial distributions in topologically similar positions to their counterparts in the mouse forebrain. For example, our analysis suggests that cell types in the goldfish Vd are putative homologs to striatal domains in mice. We identified molecular similarity between mouse MSNs and goldfish GABAergic cell types GABA26 to GABA28 and identified their zebrafish counterpart in the subpallium. MSN-like goldfish populations and the striatal marker *PENK* specifically mapped to a restricted region of the goldfish subpallium along the anterior-posterior extent of the Vd. This is further consistent with the topological correspondence of the Vd to the striatum proper (*9*, *43*, *45*).

Further, a putative homolog to the mouse retrohippocampal formation, and, in particular, the subiculum, was located in a ventral portion of the dorsolateral zone (Dlv) of the goldfish. This identification was based on molecular relation between the mouse retrohippocampal cell types together with goldfish cell types GLUT1 to GLUT3. Lesion studies implied Dlv in spatial cognition (*5*) previously, and head direction–selective cells specifically were found both in the rodent subiculum (*42*) and in the goldfish *Dlv* (*17*). This reflects an interesting correspondence between the molecular and functional level of these regions and would also be topologically consistent in light of the eversion-evagination modes of development. A similar parallel to the mammalian retrohippocampal formation was recently reported in the dorsomedial pallium of salamanders (*26*), where, aside from shared molecular signatures, mesoscale connectivity also resembled the case in reptiles and mammals.

On the other hand, similarity to other parts of the hippocampal formation was less discrete. *NEUROD6*, most strongly expressed in hippocampus CA1-2-3 in mouse, mapped to a putative horn-like shaped *Dm-Dld* region. In addition, in species comparison, we revealed similarities of mouse hippocampus proper neurons to several goldfish cell types, which appeared scattered across the Dl and Dm regions. This is reflected by contradicting observations in electric fish (*48*) and goldfish (*16*, *17*, *20*), where lesion studies and recordings of space-encoding cells linked all *Dl*, *Dm*, and even more central telencephalon to spatial cognition. Each was proposed as a teleost hippocampus homolog. We speculate that together with these functional controversies, our molecular findings point toward a less regionally bound representation of spatial behaviors than in mammals. Our results contribute a molecular axis to this body of knowledge that may aid future efforts in functional characterization. We anticipate that a multimodular approach, such as the combined use of genetic strategies with functional recordings and connectivity mapping, will bring decisive insights on conservation.

The integrated analysis of cell types mapping in their spatial context also helped us detect a putative anterior-posterior neuroanatomical twist: Moving from anterior to posterior, two groups of molecularly related cell types transitioned from *Dm-Dld* and *Dl-pDm*. This would have been missed on the basis of pure cytoarchitectural methods and emphasizes a need for more refined spatial mapping. Additional validation for this structural observation would ideally require a more seamless, full-volume method able

to multiplex enough genes to detect multiple relevant cell types. Since each of the cell type groups are also distinctly marked by the expression of *NEUROD6* (*Dm-Dld*) and *PVALB* (*Dl-pDm*), this could aid their initial functional exploration. For example, it is tempting to speculate whether the twisted structure of these compartments may have contributed to the controversy on the location of a functional goldfish counterpart to the hippocampal formation, as discussed above. We suggest that new evidence needs to take into account the precise anterior-posterior alignment and, ideally, combine functional measurements with genetic markers, such as *NEUROD6* (a hippocampus marker in mouse) and *PVALB* in the above example.

Not all cases of molecular similarity however were unambivalent examples for homologies. For example, the dopaminergic cell type GABA15 (*TH*$^+$*SLC6A3*$^+$) was correlated with dopaminergic populations of the mouse olfactory bulb (Fig. 6D and fig. S7), but other dopaminergic populations (e.g., of the mouse midbrain) were not compared. *th1* was described in a similar position in zebrafish (*30*), but unlike in the zebrafish, the goldfish telencephalon is separate from the bulb. The similarity of these dopaminergic types is therefore a potential case of molecular convergence without support in shared function or topology. Like in zebrafish, we also describe inconsistencies in the expression of many genes that mark the developmental niches of interneurons in the MGE and CGE of the mouse and other tetrapods.

In one particularly notable example that contrasted the mouse, populations of neuropeptide *SST*-expressing interneurons formed an entirely homogenous ventral nucleus, which we annotated *Vsst*. *Sst* neurons in the mouse forebrain function as inhibitory interneurons to cortical and hippocampal pyramidal cells. However, the nucleus-like aggregation of their goldfish counterparts further challenges parallels to their mouse function as local inhibitory cells. Therefore, the *Vsst* and other *SST* cells could be of great interest for further exploration to uncover to what extent this distinct cell type was evolutionary conserved in function and behavior.

The mapping of cell types between goldfish and mouse allowed us to spot possible molecular homologies between brain regions of the two species. Despite their vast evolutionary distance, the plethora of information available about mouse neuroanatomy and cell types enabled us to put the findings in goldfish in a wider neuroethological context. This effort allowed us to identify critical components that were preserved along brain evolution. Note that this information does, of course, not fully describe homologies: We do not follow the developmental nor evolutionary path of each region, and crucial knowledge that relates cell types to regional connectivity (*44*) needs to be generated in a separate effort. However, our approach does not merely test for expression of isolated, selected marker genes but molecularly defined cell types that represent functional components of the goldfish telencephalon.

Collectively, our findings provide a deep analysis of the cellular profile and transcriptional architecture of the teleostean telencephalon to reveal neuroevolutionary similarity with mammalian vertebrate forebrains. We believe that the combined neuroanatomical map, with molecular cell type information, will be of great use for deeper characterization of the regions' functions. Nevertheless, our dataset is by no means exhaustive, and the continued development of technology will result in deeper and better spatially resolved teleost atlases in the future. In addition, the role of goldfish transcript paralogs that resulted from the additional genome duplications could likely be addressed more thoroughly in the future and add important perspectives on the evolution of neo- or subfunctionalizations (*49*).

To stimulate future study of goldfish, we established an accessible web resource for free exploration of gene expression across cell types and spatial context. The data and this resource could be of value for the goldfish, zebrafish, and teleost research community and open other layers in vertebrate comparative neuroscience. For example, specific populations may be targeted genetically and/or spatially for recordings during behavioral tasks. In this context, the goldfish is of particular interest, not least due to its large size, and ease in experimental handling. Goldfish are now distributed throughout natural waters around the world, which could further facilitate comparisons of experimentally acquired data to real-world behaviors in natural water bodies (*10*). Then, studying the neurobiology of goldfish not only sheds light on their remarkable capabilities but also enhances our understanding of fundamental brain functions that transcend species boundaries.

MATERIALS AND METHODS

Animal use

We used female and male adult goldfish of late adult stage, 13 to 15 cm, housed under standard conditions in the aquarium. Experiments were conducted at the same zeitgeber time. All experimental procedures followed the legislation under the Israel Ministry of Health Animal Experiments Council and were approved by the institutional Animal Experiments Ethics Committees at the Technion Israel Institute of Technology and Ben Gurion University of the Negev.

Brain collection for scRNA-seq and Visium ST

Goldfish were euthanized using an overdose of MS-222, followed by transcardial perfusion with freshly prepared, ice-cold, carboxygenated *N*-methyl-D-glucamine (NMDG)–based artificial cerebrospinal fluid (aCSF; 93 mM NMDG, 2.5 mM KCl, 1.2 mM NaH_2PO_4, 30 mM $NaHCO_3$, 20 mM Hepes, 25 mM D-glucose, 5 mM Na-ascorbate, 2 mM thiourea, 3 mM Na-pyruvate, 10 mM $MgSO_4$, and 0.5 mM $CaCl_2$, adjusted to pH 7.3 to 7.4 with concentrated HCl) (*50*). Brains were quickly removed, maintained on ice in aCSF, and superficial meninges and vasculature removed.

Dissection, cell dissociation, and scRNA-seq

For scRNA-seq, a total of 10 goldfish were sampled on three experimental days. Microdissections followed rough anatomical borders within the telencephalon (anterior, lateral, medial, and ventral; see Fig. 1 and fig. S1). On each experimental day, several brains were microdissected in parallel and pooled such that more than one brain, and experimental day, contributed to each dissection.

After brain extraction (above), the aCSF-perfused brains were quickly embedded in 1.5% low melting temperature agarose, cooled, mounted on a Leica VT1200S Automated Vibrating Microtome, and sectioned to 500-μm coronal slices (Fig. 1B). Sections were then quickly microdissected in cold aCSF. Microdissected tissue pieces were digested in 800 to 1000 μl of papain digest solution (Worthington Papain system, vial 2 reconstituted in 5 ml of aCSF) and 5% deoxyribonuclease (DNase) (vial 3 reconstituted in 500 μl of aCSF) for 20 to 25 min at 34°C, until mechanical trituration with a wide-diameter fire-polished glass pipette easily

separated most of the tissue. Next, the remaining undigested pieces were removed by filtering the suspension through an aCSF-equilibrated 30-μm cell strainer (Partec CellTrix) to a bovine serum albumin (BSA)–coated microcentrifuge tube. Cells were pelted 200*g* for 5 min at 4°C and resuspended in 200 μl of aCSF with 2.5% DNase I (Worthington Papain system, vial 3 reconstituted in 500 μl of aCSF). For myelin and debris removal, the suspension was layered on top of 1 ml of 5% OptiPrep (Sigma-Aldrich) in aCSF in a BSA-coated microcentrifuge tube and centrifuged at 150*g* for 6 min at 4°C, with slow ramping. The resulting cell pellet was resuspended in a minimal volume of aCSF and inspected in a Burker counting chamber for intact cell morphologies and high viability and successful debris removal. At all steps, from perfusion to final single-cell suspension, tissue or cells were maintained in ice-cold carboxygenated (95% O_2 and 5% CO_2) aCSF—with the exception of papain digest, where the temperature was 34°C.

Single-cell suspensions were diluted to 1000 cells/μl and processed for 10x Chromium NextGEM generation and scRNA-seq. We followed the manufacturer's instructions, targeting 5000 to 6000 cells per sample. Sequencing libraries were multiplexed and sequenced on Illumina NextSeq or NovaSeq platforms, targeting a depth of >35 to 40 K reads per cell.

Quantification and statistical analysis scRNA-seq

Gene ortholog assignment

The goldfish transcriptome lacks high-quality transcript annotations, which hinders identification of cell types and cross-species analysis (here, mouse and goldfish). Therefore, we assigned mouse gene orthologs to the goldfish transcriptome that we used for all analysis, except zebrafish comparison (Fig. 7), where we assigned zebrafish orthologs (see below). Gene ortholog assignment was performed as follows.

For mouse, we identified gene orthologs from protein sequence, using eggnog-mapper with the EggNOG (v.5.0) orthology data (*51*). We additionally used BLASTP (*52*) with BLOSUM45 matrix to identify orthologs using protein sequences, selecting the gene with the highest score. The results from both analyses and the annotation of National Center for Biotechnology Information (NCBI) were compared and combined. Genes that were found as the same orthologs in both methods got the ortholog's name, genes found just in BLAST got the gene name from BLAST, and genes with annotations from NCBI received the gene name from the NCBI annotations. Genes with conflict in orthology between the methods received the serial number from NCBI. Most genes had one or more orthologs, and genes where no orthologs or annotations were found were excluded from further analysis. For cross-species analysis with zebrafish, we used the zebrafish transcriptome to identify gene orthologs from protein sequence, using eggnog-mapper with the EggNOG (v.5.0) orthology data (*51*) only.

Last, we verified that at the current sampling depth, goldfish gene paralogs derived from whole-genome duplications resulted in no additional cell type diversity compared to mouse annotations (fig. S2). Therefore, we collapsed (summed) reads coming from paralogs in the orthologs assignment and used this new set of genes for all further analysis. Summing also averaged noise and facilitated pairwise correlation analysis between expressions of orthologs across species.

Preprocessing and filtering

scRNA-seq data were aligned to the goldfish reference genome and transcriptome (NCBI Assembly ASM336829v1), and the mRNA molecules were counted using the 10x Genomics Cell Ranger (version 5.0.1) (*53*). Molecule count data from all sequencing runs were merged into one single database that included metadata about each cell. Cells with <500 unique molecular identifiers (UMI) s or <100 expressed genes were removed. This resulted in 75,890 valid cells. The expression of paralog genes were summed into one gene. This resulted in 21,427 genes. For normalization and noise reduction, we used mean-centering, normalization to a common molecule count, standardization (division by the SD), and log transformation.

Features selection and dimensionality reduction

With any type of clustering, the choice of feature space is crucial. Highly variable genes (features) were selected, 543 genes, using coefficient of variance (CV) as a function of mean (*54*). Genes detected in fewer than 20 cells or more than 60% of all cells will be marked invalid and will not be used in the analysis of the highly variable genes selection; in addition, we excluded the immediate early genes. Briefly, we calculated $\log_2$ of mean and $\log_2$ of CV per gene, and then we fitted a linear line to the data using linear regression and selected the genes having the greatest offset from the fitted curve; this would correspond to genes with higher-than-expected variance. The number of the selected genes (cutoff) for the analysis was determined using "elbow plot," a common heuristic to choose a cutoff point. Then, for dimensionality reduction, principal components analysis (PCA) was used on the basis of the highly variable genes. The number of the principal components (PCs) used for the downstream analysis was determined using elbow plot, 22 PCs.

Clustering and classification

Clustering of all cell at once is suitable for finding major cell types but not optimal for finding finer subdivisions among cells of the same kind (e.g., interneurons in a dataset containing both neurons, vascular cells and glia). We decided to use a multilevel clustering approach—first splitting the cells by major class and then splitting the major classes into subclass; the clusters were annotated on the basis of known cell type–specific markers. In each level, the feature space was selected according to the entire set of cells projected by PCA. To exclude batch effects and technical effects from biological ones, we run the Harmony (*38*) on the PCA, an algorithm that projects cells into a shared embedding in which cells are grouped by cell type rather than dataset-specific conditions, thus obtaining a new PCA. 2D embedding using *t*-distributed stochastic neighbor embedding (t-SNE) was performed on the PCA space. Then, the cells were clustered on the basis of their distance in 2D using the density-based spatial clustering of applications with noise (DBSCAN) nonparametric algorithm (*55*).

Level 1. We pooled samples by tissue and performed preprocessing, clustering, classification, gene enrichment, and marker gene detection (see below for details on these procedures).

Level 2. We split cells by major class and manually annotated clusters to indicate major classes of cells: neurons, glutamatergic excitatory and GABAergic inhibitory, and nonneurons. We also manually identified and removed clusters that were clearly doublets between these major classes (e.g., vascular-neurons) and clusters that were of poor quality.

Level 3. We split cells from the major classes into subclasses separately using the same analysis steps as for levels 1 and 2. Highly

variable genes and PC number were selected separately for each class: GLUT, 335 genes and 29 PCs; GABA, 409 genes and 24 PCs; nonneuronal, 483 genes and 23 PCs. Last, we performed manual inspection to remove the remaining doublet clusters and merge oversplit clusters that lacked clearly defining gene expression differences. To create the final consolidated dataset, we extensively annotated and named each cluster according to enriched genes and known cell type–specific markers. Level 3 analysis was the basis for all downstream analysis on the final 40,161 cells.

ST Visium (10x Genomics)

For ST, freshly perfused brains were quickly coated, cryomold-embedded in cryoprotectant [(OCT), TissueTek], and flash-frozen in isopentane equilibrated on dry ice. We maintained brains in sealed bags at −80°C until processing. Per brain, we collected eight left-hemisphere coronal cryosections at 10 μm in thickness, aiming at approximately 200 to 300 μm in spacing, spanning the anterior-posterior axis of the telencephalon, onto the Visium ST gene expression slide (four capture areas, 10x Genomics). For tissue preparation, we followed the manufacturer′s instructions, with the following specifications: methanol fixation; immunofluorescence staining with 4′,6-diamidino-2-phenylindole (DAPI) only (no antibody); imaging at 10× magnification on a Nikon Eclipse Ti2: differential interference contrast, DAPI, and tetramethyl rhodamine isothiocyanate channels for fiducial and section alignment; and 25-min permeabilization, as we had previously determined on test sections, using the Tissue Optimization kit. We then proceeded with the Visium Gene Expression Kit following the manufacturer′s instructions, with 15 polymerase chain reaction cycles for cDNA amplification. Sequencing was performed on Illumina NGS platforms to a depth of 150 to 200 million reads per sample (i.e., capture area or section).

Spatial analysis

With the exception of the spatial barcodes instead of cell barcodes (spots instead of cells), most of the steps are similar to scRNA-seq analysis pipeline and discussed in detail in the single-cell analysis section. Briefly, after preprocessing, filtering, normalizing, and feature selection, we perform dimensionality reduction by PCA for the high-dimensional data that we get from the sequencing output, followed by 2D embedding with t-SNE based on their similarity in the high-dimensional gene expression space. This resulted in a 2D map. Focusing on neuronal markers, we clustered these spots according to their distance in 2D using the DBSCAN algorithm. Thus, spots with similar gene expression are grouped together in the same cluster.

We also use KNN to regroup the outlier spots from the DBSCAN algorithm into their closest neighbor cluster. Afterward, these spots could be remapped to their original location on the tissue based on the spatial barcode index to test whether clusters had an unbiased spatial distribution in the tissue.

scRNA-seq integration to ST

ST spots contain RNA transcripts from multiple cells rather than single cells; hence, we need to deconvolute this mixture of cells to compare it with scRNA-seq–annotated cell type data. We then conduct a feature selection of highly variable genes for scRNA-seq and ST dataset alone, and then we combine and intersect the two feature selection gene lists together and normalizing both datasets. To calculate mapping score for each cell type per Visium spot, we used the precalculated top 10 enriched genes per cell type. For each spot, the sum of these top 10 genes was calculated and then was smoothed via sigmoid transform to enhance contrast. The output is a mapping score per cell type that can be visualized such as in fig. S5.

We then map those scores in the original positional location in the actual *X*-*Y* position of the section. We also create a weighted colormap for the sections (based on the same color map of the single cell types) using the weighted score of all cell types in all spots (Fig. 2A). To visualize a global pattern comparison, we normalize the values of the mapping score and present all the section spots together in a heatmap form.

Our approach for mapping the cell type is simple, but its meaning is very clear. To compare our results with leading published algorithms, we run the same data using the RTCD package (*56*). The results were consistent, as shown in fig. S4.

Axial spatial genes scoring

The spatial scoring values are based on the normalized SD of the gene expression of each expressed gene in the goldfish telencephalon from the centroid mean *XYZ* axes of the Visium section spots; we found a clustered pattern of selected top highly axial genes. Spatial axial score for each gene was calculated as follows, for mediolateral σ(*x*) and dorsoventral σ(*y*)

$$\sigma = \sqrt{\frac{\sum (x_i - \mu)^2}{N}}$$

where σ indicates the specific required gene SD, *N* indicates the number of spots with required gene expression in each Visium section, x_i indicates each expression value of the required gene in the Visium section, and μ indicates axial centroid mean of *X* or *Y* axis for all spots in the individual Visium section.

We also calculated the combined overall axial spatial score for both mediolateral and dorsoventral axes scores together

$$\sigma_{x-y} = \sqrt{{\sigma_x}^2 + {\sigma_y}^2}$$

Cross-species comparison and data integration

After annotating cell types, we integrated our goldfish taxonomy with our published mouse telencephalon cell type taxonomy [Zeisel *et al.* (*33*)] alone (INTEG1) or in addition, a dataset on mouse amygdala [Hochgerner *et al.* (*32*)] (INTEG2) using the data integration tool Harmony (*38*), separately for each main cell classes—GABA neurons, GLUT neurons, and nonneuronal cells. First, we randomly sampled 200 cells per cell type from each species. Then, we concatenated the two species′ datasets, normalized them, and removed genes that were not intersected between the two species, resulting in 14,010 intersected genes. Then, we selected 2000 highly variable genes from each species individually and combined the two gene lists for feature selection (see "Feature selection") with the following PCs: INTEG1 GLUT, 11; INTEG1 GABA, 15; NONNEURONAL, 11; and INTEG2 GABA, 6. Next, we normalized the merged datasets and performed dimensionality reduction in PCA space to exclude batch effect and technical effects from biological ones. Then, we performed Harmony in PCA space. Here, we implemented optimization and control measures to ensure

controlled integration and convergence of the data, as follows: Within each iteration of Harmony, we calculate the mean Euclidean distance between the new and previous projections, monitoring the changes in distance between consecutive PCA projections. This allowed us to determine a cutoff point where integration has relatively converged, preventing overintegration (elbow plot in fig. S7). This projected cells into a shared embedding in which cells are grouped by cell type rather than dataset-specific conditions and resulted in a new PCA that accounts for experimental factors, but not biological ones. We then proceeded with two methods to aid in the comparative analysis of goldfish and mouse cell types: DBSCAN clustering and KNN.

In the KNN approach, goldfish cells were classified for their *k*-nearest mouse cell neighbors in the PCA space, where we calculated the fraction of each specific cell type according to their shared mouse cell type that they were classified to. All KNN classifiers presented used $k = 25$ (where k is the number of mouse cell neighbors), although testing different k values (10, 50, and 100) did not majorly affect classification fractions, which remained stable.

In the clustering approach, the new PCA space was then embedded in *t*-SNE and clustered using DBSCAN algorithm. Similar cell types of both species fell in close proximity to their counterparts in the Euclidean 2D space embedding. Last, we calculated the percentage of each cell type in each of the integrated clusters and sorted the cell type according to their percentage values. When a mouse cell type has high similarity or analogy to a goldfish cell type, we expect a high percentage for both in an integrated cluster.

For integration with the adult zebrafish dataset (INTEG3) [Pandey *et al.* (*46*)], we followed the same logic. However, since the zebrafish dataset was not annotated by neurotransmitter class, we performed integration for the full neuronal datasets, i.e., zebrafish and goldfish GLUT and GABA cells at once. The concatenated gene list contained 11,604 intersected genes (note that this list contains collapsed paralogs). In INTEG3, feature selection was performed using six PCs.

HCR RNA–FISH

For hybridization chain reaction (HCR) RNA–FISH protocol (Molecular Instruments) for fresh frozen tissue sections was performed according to the manufacturer's instructions. All probes were designed on the basis of the main expressed paralog, except for *NEUROD6*, where sections shared by the three paralogs' sequences were targeted (i.e., *PENK*, LOC113074268; *SST*, LOC113115526; *VIP*, LOC113057506; *NEUROD6*, LOC113113148, LOC113042538, and LOC113092803; and *CBLN1*, LOC113061475; see table S1), using a custom MATLAB script (*57*). Sections were imaged on a Nikon Eclipse Ti2 epifluorescence microscope at ×10 (*CBLN1*) and ×20 magnifications.

In addition, to optimally view the HCR probes expression in section overviews, we present virtual expression of the HCR channel: In each HCR gene expression channel, we first calculated the 95th (for *CBLN1*) or 99th (for all the other HCR probes used) percentile value of the main image and segmented the binary image by thresholding the image based on this percentile value. We then performed image erosion, computed maximum intensity and centroids, and discretized values into bins with a color map.

Supplementary Materials

This PDF file includes:
Figs. S1 to S9
Legend for table S1

Other Supplementary Material for this manuscript includes the following:
Table S1

REFERENCES AND NOTES

1. C. Salas, C. Broglio, F. Rodríguez, Evolution of forebrain and spatial cognition in vertebrates: Conservation across diversity. *Brain Behav. Evol.* **62**, 72–82 (2003).
2. C. Broglio, F. Rodríguez, A. Gómez, J. L. Arias, C. Salas, Selective involvement of the goldfish lateral pallium in spatial memory. *Behav. Brain Res.* **210**, 191–201 (2010).
3. T. Fremouw, P. Jackson-Smith, R. P. Kesner, Impaired place learning and unimpaired cue learning in hippocampal-lesioned pigeons. *Behav. Neurosci.* **111**, 963–975 (1997).
4. J. C. López, F. Rodríguez, Y. Gómez, J. P. Vargas, C. Broglio, C. Salas, Place and cue learning in turtles. *Anim. Learn. Behav.* **28**, 360–372 (2000).
5. F. Rodríguez, J. C. López, J. P. Vargas, Y. Gómez, C. Broglio, C. Salas, Conservation of spatial memory function in the pallial forebrain of reptiles and ray-finned fishes. *J. Neurosci.* **22**, 2894–2903 (2002).
6. A. B. Butler, W. Hodos, *Comparative Vertebrate Neuroanatomy: Evolution and Adaptation* (John Wiley & Sons, 2005).
7. G. F. Striedter, R. G. Northcutt, *Brains through Time: A Natural History of Vertebrates* (Oxford University Press, 2019).
8. T. Mueller, M. F. Wullimann, An evolutionary interpretation of teleostean forebrain anatomy. *Brain Behav. Evol.* **74**, 30–42 (2009).
9. M. F. Wullimann, T. Mueller, Teleostean and mammalian forebrains contrasted: Evidence from genes to behavior. *J. Comp. Neurol.* **475**, 143–162 (2004).
10. K. G. Ota, *Goldfish Development and Evolution* (Springer, 2021).
11. C. Neumeyer, Tetrachromatic color vision in goldfish: Evidence from color mixture experiments. *J. Comp. Physiol. A* **171**, 639–649 (1992).
12. K. Wyzisk, C. Neumeyer, Perception of illusory surfaces and contours in goldfish. *Vis. Neurosci.* **24**, 291–298 (2007).
13. L. Lord, J. Bond, R. R. Thompson, Rapid steroid influences on visually guided sexual behavior in male goldfish. *Horm. Behav.* **56**, 519–526 (2009).
14. J. C. Beck, E. Gilland, D. W. Tank, R. Baker, Quantifying the ontogeny of optokinetic and vestibuloocular behaviors in zebrafish, medaka, and goldfish. *J. Neurophysiol.* **92**, 3546–3561 (2004).
15. E. Aksay, I. Olasagasti, B. D. Mensh, R. Baker, M. S. Goldman, D. W. Tank, Functional dissection of circuitry in a neural integrator. *Nat. Neurosci.* **10**, 494–504 (2007).
16. L. Cohen, E. Vinepinsky, O. Donchin, R. Segev, Boundary vector cells in the goldfish central telencephalon encode spatial information. *PLoS Biol.* **21**, e3001747 (2023).
17. E. Vinepinsky, L. Cohen, S. Perchik, O. Ben-Shahar, O. Donchin, R. Segev, Representation of edges, head direction, and swimming kinematics in the brain of freely-navigating fish. *Sci. Rep.* **10**, 14762 (2020).
18. J. O'Keefe, J. Dostrovsky, The hippocampus as a spatial map: Preliminary evidence from unit activity in the freely-moving rat. *Brain Res.* **34**, 171–175 (1971).
19. E. I. Moser, M. Moser, B. L. McNaughton, Spatial representation in the hippocampal formation: A history. *Nat. Neurosci.* **20**, 1448–1464 (2017).
20. K. Saito, S. Watanabe, Deficits in acquisition of spatial learning after dorsomedial telencephalon lesions in goldfish. *Behav. Brain Res.* **172**, 187–194 (2006).
21. S. Linnarsson, S. A. Teichmann, Single-cell genomics: Coming of age. *Genome Biol.* **17**, 97 (2016).
22. D. J. Burgess, Spatial transcriptomics coming of age. *Nat. Rev. Genet.* **20**, 317 (2019).
23. R. G. Northcutt, Connections of the lateral and medial divisions of the goldfish telencephalic pallium. *J. Comp. Neurol.* **494**, 903–943 (2006).
24. N. Yamamoto, H. Ito, Visual, lateral line, and auditory ascending pathways to the dorsal telencephalic area through the rostrolateral region of the lateral preglomerular nucleus in cyprinids. *J. Comp. Neurol.* **508**, 615–647 (2008).
25. M. A. Tosches, T. M. Yamawaki, R. K. Naumann, A. A. Jacobi, G. Tushev, G. Laurent, Evolution of pallium, hippocampus, and cortical cell types revealed by single-cell transcriptomics in reptiles. *Science* **360**, 881–888 (2018).
26. J. Woych, A. O. Gurrola, A. Deryckere, E. C. B. Jaeger, E. Gumnit, G. Merello, J. Gu, A. J. Araus, N. D. Leigh, M. Yun, A. Simon, M. A. Tosches, Cell type profiling in salamanders identifies innovations in vertebrate forebrain evolution. *Science* **377**, eabp9186 (2022).

27. X. Wei, S. Fu, H. Li, Y. Liu, S. Wang, W. Feng, Y. Yang, X. Liu, Y.-Y. Zeng, M. Cheng, Y. Lai, X. Qiu, L. Wu, N. Zhang, Y. Jiang, J. Xu, X. Su, C. Peng, L. Han, W. P.-K. Lou, C. Liu, Y. Yuan, K. Ma, T. Yang, X. Pan, S. Gao, A. Chen, M. A. Esteban, H. Yang, J. Wang, G. Fan, L. Liu, L. Chen, X. Xu, J.-F. Fei, Y. Gu, Single-cell Stereo-seq reveals induced progenitor cells involved in axolotl brain regeneration. *Science* **377**, eabp9444 (2022).
28. K. Lust, A. Maynard, T. Gomes, J. S. Fleck, J. G. Camp, E. M. Tanaka, B. Treutlein, Single-cell analyses of axolotl telencephalon organization, neurogenesis, and regeneration. *Science* **377**, eabp9262 (2022).
29. D. Hain, T. Gallego-Flores, M. Klinkmann, A. Macias, E. Ciirdaeva, A. Arends, C. Thum, G. Tushev, F. Kretschmer, M. A. Tosches, G. Laurent, Molecular diversity and evolution of neuron types in the amniote brain. *Science* **377**, eabp8202 (2022).
30. A. Filippi, J. Mahler, J. Schweitzer, W. Driever, Expression of the paralogous tyrosine hydroxylase encoding genes *th1* and *th2* reveals the full complement of dopaminergic and noradrenergic neurons in zebrafish larval and juvenile brain. *J. Comp. Neurol.* **518**, 423–438 (2010).
31. V. Naef, M. de Sarlo, G. Testa, D. Corsinovi, R. Azzarelli, U. Borello, M. Ori, The stemness gene *Mex3A* is a key regulator of neuroblast proliferation during neurogenesis. *Front. Cell Dev. Biol.* **8**, 549533 (2020).
32. H. Hochgerner, M. Tibi, S. Netser, O. Ophir, N. Reinhardt, S. Singh, Z. Lin, S. Wagner, A. Zeisel, Cell types in the mouse amygdala and their transcriptional response to fear conditioning. bioRxiv 2022.10.25.513733 [Preprint] (2022). https://doi.org/10.1101/2022.10.25.513733.
33. A. Zeisel, H. Hochgerner, P. Lönnerberg, A. Johnsson, F. Memic, J. van der Zwan, M. Häring, E. Braun, L. E. Borm, G. L. Manno, S. Codeluppi, A. Furlan, K. Lee, N. Skene, K. D. Harris, J. Hjerling-Leffler, E. Arenas, P. Ernfors, U. Marklund, S. Linnarsson, Molecular architecture of the mouse nervous system. *Cell* **174**, 999–1014.e22 (2018).
34. R. A. Romanov, A. Zeisel, J. Bakker, F. Girach, A. Hellysaz, R. Tomer, A. Alpár, J. Mulder, F. Clotman, E. Keimpema, B. Hsueh, A. K. Crow, H. Martens, C. Schwindling, D. Calvigioni, J. S. Bains, Z. Máté, G. Szabó, Y. Yanagawa, M. D. Zhang, A. Rendeiro, M. Farlik, M. Uhlén, P. Wulff, C. Bock, C. Broberger, K. Deisseroth, T. Hökfelt, S. Linnarsson, T. L. Horvath, T. Harkany, Molecular interrogation of hypothalamic organization reveals distinct dopamine neuronal subtypes. *Nat. Neurosci.* **20**, 176–188 (2017).
35. S. Lugert, O. Basak, P. Knuckles, U. Haussler, K. Fabel, M. Götz, C. A. Haas, G. Kempermann, V. Taylor, C. Giachino, Quiescent and active hippocampal neural stem cells with distinct morphologies respond selectively to physiological and pathological stimuli and aging. *Cell Stem Cell* **6**, 445–456 (2010).
36. N. Diotel, L. Lübke, U. Strähle, S. Rastegar, Common and distinct features of adult neurogenesis and regeneration in the telencephalon of zebrafish and mammals. *Front. Neurosci.* **14**, 568930 (2020).
37. L. Dirian, S. Galant, M. Coolen, W. Chen, S. Bedu, C. Houart, L. Bally-Cuif, I. Foucher, Spatial regionalization and heterochrony in the formation of adult pallial neural stem cells. *Dev. Cell* **30**, 123–136 (2014).
38. I. Korsunsky, N. Millard, J. Fan, K. Slowikowski, F. Zhang, K. Wei, Y. Baglaenko, M. Brenner, P.-R. Loh, S. Raychaudhuri, Fast, sensitive and accurate integration of single-cell data with Harmony. *Nat. Methods* **16**, 1289–1296 (2019).
39. D. Morizet, I. Foucher, A. Alunni, L. Bally-Cuif, Integrative single-cell transcriptomics clarifies adult neurogenesis and macroglia evolution. bioRxiv 2023.02.27.530203 [Preprint] (2023). https://doi.org/10.1101/2023.02.27.530203.
40. N. Jurisch-Yaksi, E. Yaksi, C. Kizil, Radial glia in the zebrafish brain: Functional, structural, and physiological comparison with the mammalian glia. *Glia* **68**, 2451–2470 (2020).
41. S. Nóbrega-Pereira, N. Kessaris, T. Du, S. Kimura, S. A. Anderson, O. Marín, Postmitotic Nkx2-1 controls the migration of telencephalic interneurons by direct repression of guidance receptors. *Neuron* **59**, 733–745 (2008).
42. J. S. Taube, R. U. Muller, J. B. Ranck Jr., Head-direction cells recorded from the postsubiculum in freely moving rats. I. Description and quantitative analysis. *J. Neurosci.* **10**, 420–435 (1990).
43. T. Mueller, The Everted amygdala of ray-finned fish: Zebrafish makes a case. *Brain Behav. Evol.* **97**, 321–335 (2022).
44. J. Yáñez, M. Folgueira, I. Lamas, R. Anadón, The organization of the zebrafish pallium from a hodological perspective. *J. Comp. Neurol.* **530**, 1164–1194 (2022).
45. B. A. Porter, T. Mueller, The zebrafish amygdaloid complex–functional ground plan, molecular delineation, and everted topology. *Front. Neurosci.* **14**, 608 (2020).
46. S. Pandey, A. J. Moyer, S. B. Thyme, A single-cell transcriptome atlas of the maturing zebrafish telencephalon. *Genome Res.* **33**, 658–671 (2023).
47. A. Zeisel, A. B. Muñoz-Manchado, S. Codeluppi, P. Lönnerberg, G. la Manno, A. Juréus, S. Marques, H. Munguba, L. He, C. Betsholtz, C. Rolny, G. Castelo-Branco, J. Hjerling-Leffler, S. Linnarsson, Cell types in the mouse cortex and hippocampus revealed by single-cell RNA-seq. *Science* **347**, 1138–1142 (2015).
48. K. Allen, *Amazon Nights II: Electric Boogaloo: Neural Adaptations for Communication in Three Species of Weakly Electric Fish* (West Virginia University, 2019).
49. M. E. Shafer, A. N. Sawh, A. F. Schier, Gene family evolution underlies cell-type diversification in the hypothalamus of teleosts. *Nat. Ecol. Evol.* **6**, 63–76 (2022).
50. J. T. Ting, T. L. Daigle, Q. Chen, G. Feng, Acute brain slice methods for adult and aging animals: Application of targeted patch clamp analysis and optogenetics. *Methods Mol. Biol.* **1183**, 221–242 (2014).
51. J. Huerta-Cepas, D. Szklarczyk, D. Heller, A. Hernández-Plaza, S. K. Forslund, H. Cook, D. R. Mende, I. Letunic, T. Rattei, L. J. Jensen, C. von Mering, P. Bork, eggNOG 5.0: A hierarchical, functionally and phylogenetically annotated orthology resource based on 5090 organisms and 2502 viruses. *Nucleic Acids Res.* **47**, D309–D314 (2019).
52. S. F. Altschul, W. Gish, W. Miller, E. W. Myers, D. J. Lipman, Basic local alignment search tool. *J. Mol. Biol.* **215**, 403–410 (1990).
53. G. X. Y. Zheng, J. M. Terry, P. Belgrader, P. Ryvkin, Z. W. Bent, R. Wilson, S. B. Ziraldo, T. D. Wheeler, G. P. McDermott, J. Zhu, M. T. Gregory, J. Shuga, L. Montesclaros, J. G. Underwood, D. A. Masquelier, S. Y. Nishimura, M. Schnall-Levin, P. W. Wyatt, C. M. Hindson, R. Bharadwaj, A. Wong, K. D. Ness, L. W. Beppu, H. J. Deeg, C. M. Farland, K. R. Loeb, W. J. Valente, N. G. Ericson, E. A. Stevens, J. P. Radich, T. S. Mikkelsen, B. J. Hindson, J. H. Bielas, Massively parallel digital transcriptional profiling of single cells. *Nat. Commun.* **8**, 14049 (2017).
54. D. Grün, L. Kester, A. van Oudenaarden, Validation of noise models for single-cell transcriptomics. *Nat. Methods* **11**, 637–640 (2014).
55. M. Ester, H.-P. Kriegel, J. Sander, X. Xu, A density-based algorithm for discovering clusters in large spatial databases with noise, in *Proceedings of 2nd International Conference on Knowledge Discovery and Data Mining (KDD-96)* (Association for Computing Machinery, 1996), pp. 226–231.
56. D. M. Cable, E. Murray, L. S. Zou, A. Goeva, E. Z. Macosko, F. Chen, R. A. Irizarry, Robust decomposition of cell type mixtures in spatial transcriptomics. *Nat. Biotechnol.* **40**, 517–526 (2022).
57. S. Kanatani, J. C. Kreutzmann, Y. Li, Z. West, D. V. Nikou, J. L. Skytte, L. L. Larsen, D. H. Tanaka, D. Kaczynska, K. Fukumoto, N. Uesaka, T. Tanabe, A. Miyakawa, U. Roostalu, J. Hecksher-Sørensen, P. Uhlén, Whole-brain three-dimensional imaging of RNAs at single-cell resolution. bioRxiv 2022.12.28.521740 [Preprint] (2022). https://doi.org/10.1101/2022.12.28.521740.
58. H. W. Dong, The Allen Reference Atlas: A Digital Color Brain Atlas of the C57Bl/6J Male Mouse (John Wiley & Sons Inc, 2008).

Acknowledgments: We thank D. Sagi and L. Appelbaum for critical discussion of the data and help with the HCR protocol and R. Anadón for critical input. **Funding:** We gratefully acknowledge financial support from the following funders: A.Z. is supported by the European Research Council (TYPEWIRE-852786), Human Frontiers Science Program (CDA-0039/2019-C), and Israel Science Foundation (2028912). R.S. is supported by the Israel Science Foundation-FIRST program (555/19) and Human Frontiers Science Program (RGP0016/2019). H.H. is supported by the Swedish Brain Foundation (Hjärnfonden). T.M. is supported by the Cognitive and Neurobiological Approaches to Plasticity (CNAP), Center of Biomedical Research Excellence (COBRE) of the National Institutes of Health under grant number P20GM113109, and Human Frontier Science Program (RGP0016/2019). **Author contributions:** Conceptualization: A.Z. and R.S. Investigation: H.H., S.B.H., S.G., Z.L., O.O., and M.T. Formal analysis: M.T., S.B.H., and A.Z. Software: M.T., S.B.H., and A.Z. Supervision: A.Z., R.S., and T.S. Validation: M.T. Visualization: H.H., A.Z., M.T., and S.B.H. Writing—original draft: M.T., S.B.H., and H.H. Writing—review and editing: H.H., R.S., T.M., and A.Z. **Competing interests:** The authors declare that they have no competing interests. **Data and materials availability:** All data needed to evaluate the conclusions in the paper are present in the paper and/or the Supplementary Materials. The sequencing data generated in the current study have been deposited in the GEO database at NCBI (accession no. PRJNA1018874). All code, the final single-cell expression dataset, and ST dataset, with annotations and metadata, as well as high-resolved cell types mapping (fig. S5), are available from Dryad, DOI:10.5061/dryad.qfttdz0p9. All custom code is also available from GitHub (https://github.com/muhammadtibi/Goldfish_Telencephalon_scRNAseq). We provide an online accessible resource for gene- and cell type exploration for scRNA-seq and Visium ST data. The website is available at https://zeisellab.org/goldfish/.

Submitted 13 March 2023
Accepted 29 September 2023
Published 1 November 2023
10.1126/sciadv.adh7693